

Transparent Vision: A Theory of Hierarchical Invariant Representations

Shuren Qi Yushu Zhang* Chao Wang Zhihua Xia Xiaochun Cao Fenglei Fan

Abstract

Developing robust and interpretable vision systems is a crucial step towards trustworthy artificial intelligence. One promising paradigm is to design transparent structures, e.g., geometric invariance, for fundamental representations. However, such invariants exhibit limited discriminability, limiting their applications in larger-scale tasks.

*For this open problem, we conduct a systematic investigation of **hierarchical invariance**, exploring this topic from theoretical, practical, and application perspectives.*

At the theoretical level, we show how to construct discriminative invariants with a Convolutional Neural Network (CNN)-like hierarchical architecture, yet in a fully transparent manner. The general blueprint, specific definitions, invariant properties, and numerical implementations are provided. At the practical level, we discuss how to customize this transparent framework into a given task. With the over-completeness, discriminative features w.r.t. the task can be adaptively formed in a Neural Architecture Search (NAS)-like manner. We demonstrate the above arguments with accuracy, invariance, and efficiency results on laboratory-style classification experiments. Furthermore, at the application level, our representations are explored in real-world forensic tasks on adversarial perturbations and generated content. Such applications reveal that our invariants exhibit competitive discriminability even in the era of deep learning.

For robust and interpretable vision tasks at larger scales, hierarchical invariant representations can be considered as an effective alternative to traditional CNNs and invariants.

1. Introduction

The trustworthiness is a rising topic in modern Artificial Intelligence (AI) communities [48]. Over the past decade, deep learning techniques, especially Convolutional Neural Network (CNN), have led to breakthrough results in numerous AI tasks, e.g., processing human perceptual information [20], playing board games [36], and solving hard science problems [45]. More recently, their applications are

Table 1. A conceptual comparison with related approaches.

Approach	Traditional invariants	Traditional CNNs	Scattering networks	Equivariant networks	Hierarchical invariants
Discriminative		✓	✓	✓	✓
Robust	✓		✓	✓	✓
Interpretable	✓		✓	✓	✓
Efficient	✓		✓		✓

expanding into trust-related scenarios, e.g., biometrics [39], medical diagnostics [47], self-driving cars [10], and misinformation detection [17]. In such scenarios, the robustness and interpretability of AI systems are crucial [24]: 1) *robustness* means the performance is stable for intra-class variations on the input; 2) *interpretability* means the behavior can be understood or predicted by humans.

Integrating invariance into image representations is a transparent structure towards robust and interpretable vision systems [5]. Specifically, representations play a fundamental role in visual systems, where the system is generally built on meaningful representations of digital images (rather than the raw data) [3]. Note that the proper design/learning of such representations in fact relies on priors *w.r.t.* the task of interest [43]. Here, the concept of *symmetry* from the Erlangen Program [18, 42] may be the most fruitful prior – informally, a symmetry of a system is a transformation such that a certain property of said system is *invariant* to this transformation. Symmetry priors are ubiquitous in vision tasks, e.g., translation as a symmetry of the classification system where the object category is invariant under translation [11].

1.1. State of the Art and Motivation

Historically, to a certain extent, efforts at invariance [31] and discriminability [50] have developed independently in hand-crafted [31] and learning [50] approaches. The compatibility between invariance and discriminability has emerged as a tricky problem when moving towards trustworthy AI. (see also Section A1)

In this regard, recent advances are seeking more advanced invariant designs of image representations, e.g., geometric deep learning [5], fulfilling discriminability, robustness, and interpretability simultaneously.

- On the discriminability of hand-crafted representations, researchers introduce successful experiences be-

*Corresponding author.

hind learning representations, especially cascading and over-complete designs. One of the most representative work is Invariant Scattering Convolution Networks [6], where the classical wavelet transform is expanded into an over-complete representation with deep cascading. Unlike typical CNNs: 1) regarding the architecture, convolutional layers are defined by fixed wavelet filters, with modulus-based nonlinearity, but without subsequent pooling; 2) regarding the representation properties, the architecture yields the translation equivariance and certain robustness *w.r.t.* non-linear deformations. With similar design goals and paths, we consider Scattering Networks as a main competitor for our work. (see also [Section A2](#))

- On the robustness and interpretability of learning representations, researchers introduce successful experiences behind hand-crafted representations, especially invariance and equivariance designs. One of the most representative work is Group Equivariant Convolutional Networks [7], where the classical convolution is generalized to a new definition on the symmetry group. Unlike typical CNNs: 1) regarding the architecture, convolutional layers are learned but with new structure inspired by symmetry priors, *e.g.*, re-parameterizing the filter to control symmetry; 2) regarding the representation properties, the architecture commonly provides the joint equivariance for translation and rotation. With similar design goals but on the learning path, we consider Equivariant Networks as a secondary competitor for our work. (see also [Section A2](#))

Motivation: Despite starting from different theories, the above state-of-the-art methods exhibit common problems in the implementation efficiency and representation capability. An over-simplified interpretation on the technical level of such methods is as follows [38]: The input feature map is convolved with symmetry versions of the same filter to obtain multi-channel features, where the distortion on the input (*e.g.*, rotation) corresponds to the cyclic shift between channels, and hence the invariance is achieved by pooling across channels. 1) Regarding the implementation efficiency, this parallel framework leads to an exponential expansion on the computational size (*w.r.t.* the sampling rate on symmetry), especially for learning representations where the introduced new learnable parameters make the training more challenging. 2) Regarding the representation capability, the discrete sampling on the symmetry of filters raises a tricky trade-off between invariance and discriminability – higher sampling rate implies better invariance, but the resulting computational cost restricts the overall size of representation networks (going deeper or wider), and hence the improvement of discriminability.

1.2. Contributions

As a potential step towards solving the above open problem, we conduct a systematic investigation of *hierarchical*

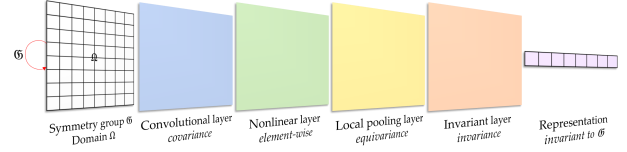


Figure 1. The blueprint of hierarchical invariance, where the image information is able to pass through each intermediate layer in a geometrically controllable manner, and on the last layer, the invariant features are allowed by compact designs, with also sufficient information.

invariance, exploring this topic from theoretical, practical, and application perspectives.

As summarized in Table 1, our approach stands nicely between the two extremes, *i.e.*, traditional invariance [31] and CNNs [50] *w.r.t.* discriminability, robustness, and interpretability. Compared with the recent scattering [6] and equivariant [7] networks, our approach is characterized by a more efficient design. Here, the equivariance is continuous/one-shot, holds across layers, eliminating the need for complex symmetry sampling, parallel framework, and cross-channel pooling. Therefore, it exhibits better efficiency, and also allowing more flexibility in enlarging the network size (going deeper or wider) to increase the representation capacity.

Theory: We formalize a blueprint for hierarchical invariance, rethinking the typical modules of CNN representations. We define new modules with their compositions to fulfill the blueprint, providing formal conclusions about the geometric symmetries between image and representation. We discuss the criticisms and developments of the above new idea versus typically concepts, highlighting our uniqueness in moving towards robust and interpretable representations.

Practice: We provide a specific framework for the theory of hierarchical invariance, covering practical principles about the topologies, layers, and parameters. We explore the data adaptability potential of the above framework, resorting to feature/architecture selection or cascading learning module.

Application: We conduct pattern classification experiments on typical sets of texture, digit, and parasite images, respectively, examining the properties promised by our theory under diverse task scales and geometric variants. We check the realistic usefulness in large-scale digital forensics of adversarial perturbation and AIGC. Here, the HIR yields consistently good discriminability, robustness, efficiency, and interpretability in a plug-and-play way, exhibiting competitive overall performance than current representation and forensic methods.

2. Hierarchical Invariance: Theory

This section focuses on the theoretical aspects of the proposed HIR. As a high-level intuition, we formalize the blueprint of hierarchical invariance, rethinking the typical modules of CNN representations. Starting from the invariant theory, we then define new modules with their compositions to fulfill such blueprint, along with representation property justifications.

2.1. Blueprint of Hierarchical Invariance

The terms of invariance, equivariance, and covariance appear in the fields of computer vision, graphics, geometry, and physics. We use the following identities to generally denote such terms [21, 28]:

- invariance — $\mathcal{R}(\mathcal{D}(f)) \equiv \mathcal{R}(f)$,
- equivariance — $\mathcal{R}(\mathcal{D}(f)) \equiv \mathcal{D}(\mathcal{R}(f))$,
- covariance — $\mathcal{R}(\mathcal{D}(f)) \equiv \mathcal{D}'(\mathcal{R}(f))$,

where \mathcal{R} is a representation, \mathcal{D} is a degradation, and \mathcal{D}' is a composite function of \mathcal{D} . Note that invariance and equivariance are special cases of covariance with $\mathcal{D}' = \text{id}$ and $\mathcal{D}' = \mathcal{D}$.

Our goal is to achieve such a CNN-like hierarchical architecture – the image information is able to pass through each intermediate layer in a geometrically controllable manner, and on the last layer, the invariant features are allowed by compact designs, with also sufficient information. In this paper, this ideal representation structure is termed as hierarchical invariance.

Motivated by the goal, we rethink typical modules of CNN representation and formalize a blueprint of such modules for hierarchical invariance, as shown in Fig. 1.

Formulation 1 (Hierarchical Invariance Blueprint). *The set of feature maps (including input images) is denoted as $X(\Omega, H) \triangleq \{M(i, j; k) : \Omega \rightarrow H\}$ with the discrete domain $(i, j) \in \Omega$ and complex-valued channels $\mathcal{C}^k \in H$, where Ω' and H' are the variants of Ω and H , respectively under certain operators, e.g., downsampling, and \mathfrak{G} is a group modeling all the symmetries of interest over Ω . We formalize the following modules for hierarchical invariance*

- **Convolutional Layer** $\mathbb{C} : X(\Omega, H) \rightarrow X(\Omega', H')$ captures local features by convolution operations. The geometric principle of \mathbb{C} is the **covariance** for the symmetry group \mathfrak{G} , i.e., there exists a predictable \mathfrak{g}' such that $\mathbb{C}(\mathfrak{g}M) = \mathfrak{g}'\mathbb{C}(M)$ for any $\mathfrak{g} \in \mathfrak{G}$ and $M \in X$, where the covariance specializes to the equivariance when $\mathfrak{g}' = \mathfrak{g}$.
- **Nonlinear Layer** $\mathbb{S} : X(\Omega, H) \rightarrow X(\Omega, H')$ introduces the non-linearity in features for discriminative purposes, with an activation function σ such that $(\mathbb{S}M)(i, j) = \sigma(M(i, j))$, where the composition of convolutional and nonlinear layers, i.e., $\mathbb{S} \circ \mathbb{C}$, is also covariant for the group \mathfrak{G} , due to the **element-wise** act of σ .

- **Local Pooling Layer** $\mathbb{P} : X(\Omega, H) \rightarrow X(\Omega', H)$ down-samples the plane dimensions of feature maps to reduce computational complexity, such that $\Omega' \subseteq \Omega$. The geometric principle of \mathbb{P} is the (approximately) **equivariance** for any \mathfrak{g}' produced by \mathbb{C} , i.e., $\mathbb{P}(\mathfrak{g}'M) \simeq \mathfrak{g}'\mathbb{P}(M)$, allowing the subsequent convolutional layer \mathbb{C} to continue capturing such covariant features, where the composition $\mathbb{P} \circ \mathbb{S} \circ \mathbb{C}$ remains covariance for the group \mathfrak{G} .

- **Invariant Layer** $\mathbb{I} : X(\Omega, H) \rightarrow Y$ obtains the final vector representation via a certain global pooling over plane dimensions. The geometric principle of \mathbb{I} is the **invariance** for the symmetry group \mathfrak{G} , i.e., $\mathbb{I}(\mathfrak{g}M) = \mathbb{I}(M)$ for any $\mathfrak{g} \in \mathfrak{G}$ and $M \in X$.

With this blueprint, HIR can be designed in a generic way, by the ordered cascading of such modules.

2.2. Definition of Layer and Path

From the foundations of invariant theory in [Section A3](#) [31, 32], we will give a class of definitions for layers \mathbb{C} , \mathbb{S} , \mathbb{P} , and \mathbb{I} , satisfying the hierarchical invariance blueprint.

Definition 1 (Convolutional Layer). *For the input feature map $M(i, j; k)$ with $\Omega = \{1, 2, \dots, N_i\} \times \{1, 2, \dots, N_j\}$ and $H = \mathcal{C}^K$, the convolutional layer \mathbb{C} is defined channel-wise as **local covariant representations** with (A3) and (A4) in [Section A3](#):*

$$\mathbb{C}M \triangleq \langle M, V_{nm}^{uvw} \rangle = M(i, j; k) \otimes (H_{nm}^w(i, j))^T, \quad (1)$$

where \otimes is the convolution over the Ω , $(\cdot)^T$ denotes the matrix transpose, and H_{nm}^w is a convolution kernel defined as:

$$H_{nm}^w(i, j) = \{h_{nm}^{uvw}(i, j) : u, v = w, (i, j) \text{ s.t. } D_{ij} \cap D \neq \emptyset\}, \quad (2)$$

where h_{nm}^{uvw} is the integral value of basis function over a valid pixel region:

$$h_{nm}^{uvw}(i, j) = \iint_{D_{ij} \cap D} (V_{nm}^{uvw}(x, y))^* dx dy, \quad (3)$$

with (i, j) -centered pixel region $D_{ij} = \{(x, y) \in [i - \frac{\Delta i}{2}, i + \frac{\Delta i}{2}] \times [j - \frac{\Delta j}{2}, j + \frac{\Delta j}{2}]\}$.

Remark. In Definition 1, the convolutional layer \mathbb{C} is specified by w and (n, m) , which control the representation scale and representation frequency of $\mathbb{C}M$, respectively. Note that the \mathbb{C} defined by (3) will directly inherit the representation properties in [Section A3](#), it should be regarded as a linear covariant layer on the group \mathfrak{G} modeling all translation, rotation, flipping, and scaling symmetries over the Ω . For convenience, we denote $\mathfrak{G} = \mathfrak{G}_1 \times \mathfrak{G}_2$, where \mathfrak{G}_1 is the translation/rotation/flipping symmetry group and \mathfrak{G}_2 is the scaling symmetry group.

Definition 2 (Nonlinear Layer). *For the input feature map $M(i, j; k)$ with $\Omega = \{1, 2, \dots, N_i\} \times \{1, 2, \dots, N_j\}$ and $H = \mathcal{C}^K$, the nonlinear layer \mathbb{S} is defined channel-wise as a magnitude operation:*

$$\mathbb{S}M = \sigma(M(i, j)) \triangleq |M(i, j; k)|, \quad (4)$$

where $M(i, j; k)$ is complex-valued, and (12) can be written explicitly as $\sqrt{(\text{Re}M(i, j; k))^2 + (\text{Im}M(i, j; k))^2}$.

Remark. With Definition 2 and Section A3, the composition of convolutional and nonlinear layers will exhibit the joint equivariance of translation, rotation, and flipping, i.e., $\mathbb{S} \circ \mathbb{C}(\mathbf{g}_1 M) = \mathbf{g}_1 \mathbb{S} \circ \mathbb{C}(M)$ for any $\mathbf{g}_1 \in \mathfrak{G}_1$ and $M \in X$. Note that \mathbb{S} defined by (4) not only introduces the non-linearity in feature maps, but also converts the covariance \mathbf{g}'_1 (from \mathbb{C} w.r.t. rotation and flipping) into the more manageable equivariance \mathbf{g}_1 . In addition, the composition $\mathbb{S} \circ \mathbb{C}$ preserves the scaling covariance of \mathbb{C} due to the element-wise act of \mathbb{S} , i.e., $\mathbb{S} \circ \mathbb{C}(\mathbf{g}_2 M) = \mathbf{g}'_2 \mathbb{S} \circ \mathbb{C}(M)$ for any $\mathbf{g}_2 \in \mathfrak{G}_2$ and $M \in X$.

Definition 3 (Local Pooling Layer). *For the input feature map $M(i, j; k)$ with $\Omega = \{1, 2, \dots, N_i\} \times \{1, 2, \dots, N_j\}$ and $H = \mathcal{C}^K$, the local pooling layer \mathbb{P} is defined channel-wise as a downsampling operation:*

$$\mathbb{P}M = M', \quad (5)$$

with $M' : \Omega' \rightarrow H$, where the local pooling layer \mathbb{P} down-samples the plane dimensions of feature maps to reduce computational complexity, such that $\Omega' \subseteq \Omega$.

Remark. According to related researches, downsampling operations (e.g., local max pooling) of CNNs will variably impair (translation) equivariance, i.e., an approximation $\mathbb{P}(\mathbf{g}M) \simeq \mathbf{g}\mathbb{P}(M)$, especially for larger pooling scales or deeper network architectures, implying a trade-off between computational complexity and representation equivariance. Since the proposed representation is one-shot without the large-scale training of typical CNNs, we neglect downsampling operations and simply set $\mathbb{P} = \text{id}$ when the computational cost is acceptable. Alternatively, more elegant pooling designs with better tradeoffs between complexity and equivariance can be employed to define \mathbb{P} , as detailed in the paper by Zhang [50]. It is straightforward that the composition $\mathbb{P} \circ \mathbb{S} \circ \mathbb{C}$ enjoys the same representation properties of $\mathbb{S} \circ \mathbb{C}$ based on Definition 3.

Definition 4 (Invariant Layer). *For the input feature map $M(i, j; k)$ with $\Omega = \{1, 2, \dots, N_i\} \times \{1, 2, \dots, N_j\}$ and $H = \mathcal{C}^K$, the invariant layer \mathbb{I} is defined channel-wise as **global invariant representations** with (A1) and (A2) in Section A3:*

$$\mathbb{I}M = \mathcal{I}(\{\langle M(i, j; k), V_{nm}(x_i, y_j) \rangle\}), \quad (6)$$

where \mathcal{I} is a special transform mapping image moments to global invariants, w.r.t. the symmetry group of interest $\mathfrak{G}_0 \subseteq \mathfrak{G}_1 \times \mathfrak{G}_2$ and any $M \in X$.

Remark. In Definition 4, we have not restricted \mathcal{I} to a fixed formula, allowing the generality of the discussion in the following Section 2.3; its specific designs (w.r.t. considered applications of this paper) will be given in Section A7. Note that, with Definitions 1 ~ 3 and Section A3, the M form $\mathbb{P} \circ \mathbb{S} \circ \mathbb{C}$ with its cascade will basically preserve the geometric information of f , specifically the translation, rotation and flipping symmetries. Therefore, the idea of \mathcal{I} (w.r.t. the deep feature map M) is very similar to the classical theory of moment invariants (w.r.t. the original image f), with a wide range of potential designs [31].

Definition 5 (Path). *From Definitions 1 ~ 4, we define a path of HIR as $p = (\lambda_{[1]}, \lambda_{[2]}, \dots, \lambda_{[L]})$, where $\lambda_{[z]} = (n, m, w)_{[z]}$ specifies the parameters of the convolutional layer sorted by z . The HIR along a path p , \mathcal{R}_p , is defined as the following ordered cascading with corresponding parameters $p = (\lambda_{[1]}, \lambda_{[2]}, \dots, \lambda_{[L]})$:*

$$\mathcal{R}_p \triangleq \mathbb{I} \circ \mathbb{P}_{[L]} \circ \mathbb{S}_{[L]} \circ \mathbb{C}_{[L]} \circ \dots \circ \mathbb{P}_{[1]} \circ \mathbb{S}_{[1]} \circ \mathbb{C}_{[1]}. \quad (7)$$

Remark. In Definition 5, we further unify the global and local representation theories of moment invariants (Section A3) into a hierarchical representation framework. Note that the layers prior to the invariant layer \mathbb{I} provide structure-preserving properties for the representation \mathcal{R}_p . Here, the global representation (7) is designed for image-level visual tasks, e.g., classification; as for pixel-level ones, e.g., segmentation, we can preserve the spatial dimensions by removing the last invariant layer. In the next section, the representation properties of Definition 5 will be analyzed.

2.3. Representation Property

In a typical CNN, the relationship between image information and learned representation is highly nonlinear and difficult to understand or predict. As for the HIR, we can explicitly give the following conclusions about the geometric symmetries between image and representation, implying good robustness and interpretability. (see Section A4 for proofs)

Property 1 (Equivariance for Translation, Rotation, and Flipping). *For a representation unit $\mathbb{U} \triangleq \mathbb{P} \circ \mathbb{S} \circ \mathbb{C}$ with arbitrary parameters λ (for the convolutional layer), any composition of \mathbb{U} satisfy the joint equivariance for translation, rotation, and flipping (ignoring edge effects and resampling errors), i.e., the following identity holds:*

$$\mathbb{U}_{[L]} \circ \dots \circ \mathbb{U}_{[2]} \circ \mathbb{U}_{[1]}(\mathbf{g}_1 M) \equiv \mathbf{g}_1 \mathbb{U}_{[L]} \circ \dots \circ \mathbb{U}_{[2]} \circ \mathbb{U}_{[1]}(M). \quad (8)$$

for any composition length $L \geq 1$, any $\mathbf{g}_1 \in \mathfrak{G}_1$ and $M \in X$, where \mathfrak{G}_1 is the translation/rotation/flipping symmetry group.

Property 2 (Covariance for Scaling). *For a representation unit \mathbb{U} , where the scale parameter of its convolutional layer is specified as w with a notation $\mathbb{U}^w \triangleq \mathbb{P} \circ \mathbb{S} \circ \mathbb{C}^w$, any composition of \mathbb{U}^w satisfy the covariance for scaling (ignoring edge effects and resampling errors), i.e., the following identity holds:*

$$\begin{aligned} & \mathbb{U}_{[L]}^w \circ \cdots \circ \mathbb{U}_{[2]}^w \circ \mathbb{U}_{[1]}^w(\mathbf{g}_2 M) \\ & \equiv \mathbf{g}'_2 \mathbb{U}_{[L]}^w \circ \cdots \circ \mathbb{U}_{[2]}^w \circ \mathbb{U}_{[1]}^w(M) \\ & = \mathbf{g}_2 \mathbb{U}_{[L]}^{ws} \circ \cdots \circ \mathbb{U}_{[2]}^{ws} \circ \mathbb{U}_{[1]}^{ws}(M), \end{aligned} \quad (9)$$

for any composition length $L \geq 1$, any $\mathbf{g}_2 \in \mathfrak{G}_2$ and $M \in X$, where \mathbf{g}'_2 is a predictable operation corresponding to \mathbf{g}_2 with explicit form $\mathbf{g}'_2 \mathbb{U}^w \triangleq \mathbf{g}_2 \mathbb{U}^{ws}$, s is the scaling factor w.r.t. \mathbf{g}_2 , and \mathfrak{G}_2 is the scaling symmetry group.

Property 3 (Hierarchical Invariance). *For any composition of representation unit \mathbb{U} , it is practical to design a global invariant map \mathbb{I} w.r.t. the symmetry group of interest $\mathfrak{G}_0 \subseteq \mathfrak{G}_1 \times \mathfrak{G}_2$, due to the predictable geometric symmetries between the input image and deep feature map (at each intermediate layer) guaranteed by Properties 1 and 2. More specifically, with Definition 4, we assume that there exists an \mathbb{I} such that $\mathbb{I}(\mathbf{g}_0 M) = \mathbb{I}(M)$ for any $\mathbf{g}_0 \in \mathfrak{G}_0$ and $M \in X$, i.e., invariance holds on one layer, where \mathbf{g}' is a predictable operation corresponding to \mathbf{g} and \mathbb{U} . Then we have following invariance:*

$$\mathbb{I}(\mathbf{g}'_0 M)_{[L]} \equiv \mathbb{I}M_{[L]}, \quad (10)$$

holds for any composition length $L \geq 1$.

For a summary of this theoretical section, we discuss the criticisms and developments of the proposed idea versus typically concepts in [Section A5](#).

3. Hierarchical Invariance: Practice

This section focuses on the practical aspects of the proposed HIR. Note that such efforts only serve as a feasible practice of hierarchical invariance theory, towards the experiments and applications in [Section 4](#).

We discuss practical details on numerical implementations, network parameters, layer settings in [Section A6](#).

3.1. Specifying the Architecture

Starting from Properties 1 ~ 3, we propose a practical architecture for the hierarchical invariance w.r.t. the symmetry group of interest $\mathfrak{G}_0 = \mathfrak{G}_1 \times \mathfrak{G}_2$, with a tree topology and working at multiple scales.

Single-scale Networks: Let us first present the topology on a single scale, i.e., all involved convolutional layers have a common scale parameter w , which exhibits invariance for \mathfrak{G}_1 (Properties 1 and 2). As shown in Fig.

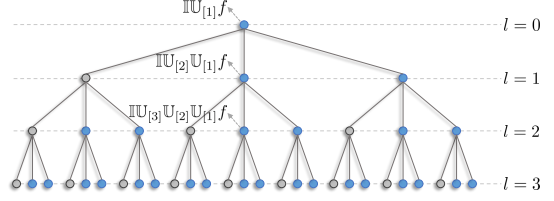


Figure 2. A single-scale practice of HIR with \mathfrak{G}_1 invariance.

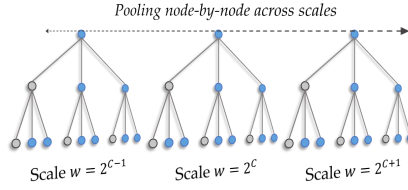


Figure 3. A multi-scale practice of HIR with \mathfrak{G}_0 invariance.

2, we organize the set of paths as a tree-like network: 1) blue nodes denote the representation units \mathbb{U} with different parameters (n, m) ; 2) black nodes denote the identity function; 3) lines denote cascading relationships between nodes, where all nodes sorted by l along their paths are plotted at the same level l (sorted from top to bottom). Note that the feature map of each node will be fed into \mathbb{I} for forming the invariants under this path, where the network representation is just the set of invariants under all paths.

Multi-scale Networks: Next, let us consider a multi-scale version of the above network with scale separation prior, extending the invariance to \mathfrak{G}_0 (Property 3). As shown in Fig. 3, a series of single-scale networks are introduced: 1) they have the same tree topology and same order parameter at corresponding nodes; 2) but each network has a different scale parameter, sampled from the set $\{w : w = 2^t, t \in \mathbb{Z}\}$, where the scaling covariance (w.r.t. w) is transformed into a linear translation pattern (w.r.t. t) between multi-scale networks. The above network can derive a series of multi-scale representations of the image (with invariance for \mathfrak{G}_1), which are directly suitable for visual tasks with multi-scale physical structure (e.g., object detection). Further, we can derive scale-invariant representations (with invariance for \mathfrak{G}_0) under Property 3, by pooling feature maps from a series of corresponding nodes at multiple scales. Note that, in practice, we cannot sample the scale completely and densely, and thus the above scaling invariance is restricted.

3.2. Empowering the Data Adaptability

Due to the hand-crafted nature of HIR, a fixed set of their features is not adaptive to the data distribution. For larger-scale vision tasks, we propose following data adaptability strategies, allowing our invariants to reach a similar discriminability level of learning representations. Note that

unlike typical (under)-complete invariants, our invariants exhibit a high level of over-completeness due to the local and hierarchical structure, which is the foundation for data adaptability strategies.

Feature/Architecture Selection: Discriminative features for a given task can be formed in a selection-based manner, inspired by Neural Architecture Search (NAS) [2]. First, we can construct a large-scale tree-like network (going deeper or wider), covering a wide set of paths and parameters, analogous to the notion of supernet in NAS [14]. Then, with the training set under a given task, we can perform correlation analysis of features and labels for ranking discriminative features (as well as the corresponding paths), analogous to the phase of architecture sampling and evaluation in NAS [14]. With the above analysis, we can greatly simplify the initial supernet such that the paths cover top-ranked features for applications, allowing our representations to be task-discriminative.

Cascading Learning Module: Discriminative features for a given task can also be formed in a learning-based manner, inspired by Hybrid Representation Learning (HRL) [30]. The main idea is to replace shallow layers of learning CNNs with a fixed HIR, such that discriminative features are formed in a space with geometric symmetries. According to related justifications [30], this strategy is able to achieve a discriminability-level rivaling typical CNNs on large-scale classification benchmarks, while exhibiting significantly better training compactness. In all experiments and applications of this paper, we still employ the feature/architecture selection strategy to show the superiority of the hierarchical invariant framework itself, taking also into account that the cascading CNN weakens invariance and interpretability to some extent.

4. Experiments and Applications

In this section, we will comprehensively evaluate the discriminability, robustness, and efficiency of HIR, covering simulation experiments in Section 4.1 and real-world applications in Section 4.2. Here, the main aim is for examining the representation properties promised in previous sections, as well as positioning its discriminative power in the era of deep learning. (see [Section A7](#) for implementation details)

4.1. Simulation Experiments

We perform classification experiments with HIR on typical sets of digit, texture, and parasite images, benchmarking its representation capabilities. We have moved the experiments on texture and parasite images to [Section A8](#) due to space constraints. Note that this series of simulation experiments examines the properties promised by our theory under diverse task scales and geometric variants, also with comparisons to a range of hand-crafted and learning representations.

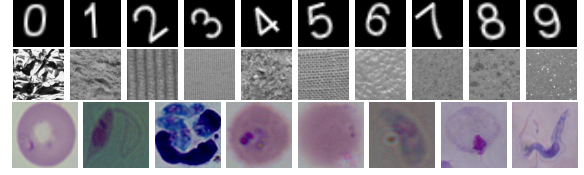


Figure 4. Illustration for the datasets from simulation experiments.

Table 2. Classification scores (%) and runtime (second) for different representations on a digit benchmark.

Method	Time GPU†	Original			Trans. & Rota.		
		Pre.	Rec.	F1	Pre.	Rec.	F1
<i>Classical:</i>							
Cosine	15	45.68	45.35	45.43	32.50	31.20	30.83
Wavelet	16	67.11	66.75	66.75	38.31	35.25	35.44
Kraw.	15	71.73	69.85	69.69	27.05	26.30	25.83
<i>Learning:</i>							
SimpleNet	535†	98.60	98.60	98.60	35.42	33.50	33.72
SimpleNet+	551†	52.70	48.90	48.82	54.26	50.75	50.78
AlexNet	393†	100	100	100	66.18	64.45	64.27
AlexNet+	392†	93.07	92.00	91.80	94.23	93.10	92.93
VGGNet	3610†	100	100	100	70.74	70.25	69.93
VGGNet+	7731†	95.98	95.70	95.68	95.53	95.20	95.13
<i>Invariant:</i>							
ScatterNet	115	98.96	98.95	98.95	57.20	56.95	56.23
HIR	57	97.48	97.45	97.45	95.05	94.95	94.98

The competing representations involved here can be summarized as follows:

- Classical complete representation: discrete cosine transform as a global representation;
- Classical over-complete representation: discrete wavelet transform [27] and Krawtchouk moments [49] as local representations of different time-frequency resolutions;
- Advanced over-complete representations: 1) typical CNNs, *i.e.*, direct-learning CNNs (denoted as SimpleNet), transfer-learning AlexNet [19] and VGGNet [37], with also data augmentation (denoted as '+'); 2) invariant CNNs, *i.e.*, scattering networks [6] and our HIR. They can all be considered as a class of hierarchical invariant representations, but with different invariances, where typical CNNs are invariant only to translations.

As shown in Fig. 4, the experiment is executed on a digit dataset¹ for classification similar to the MNIST benchmark. This dataset has 10 classes from ‘0’ to ‘9’, each containing 1000 instances with rich font differences and geometric distortions, the total size is $10 \times 1000 = 10000$.

As shown in Table 2, we list performance scores and elapsed times of the competing representations on this benchmark. Besides this direct protocol, we also consider testing image variants with random translation (*w.r.t.* $-2 \sim 2$ pixels in axial directions) and random rotation (*w.r.t.* $0 \sim 360$ degrees around the center).

¹<https://ww2.mathworks.cn/help/deeplearning/ug/data-sets-for-deep-learning.html>



Figure 5. Illustration for the datasets from forensic applications.

- The classical representations fail to achieve a satisfactory level of discriminability. Here, the complete Cosine exhibits the worst scores, while the over-complete Wavelet and Krawtchouk perform better, revealing the role of over-completeness in the discriminability. Regarding robustness, such representations all fail against translation and rotation variants, implying the challenging nature of this protocol.
- In general, the learning CNN family achieves significantly higher scores due to its over-complete and data-adaptive properties, but also with the sensitivity of learning to network size, training strategy, and geometric variants. Its robustness is significantly increased after augmented training. However, theoretically, the resulting robustness is not guaranteed for unseen data distributions (even for similar variants with unseen parameters). One can note the rapid expansion of computational cost: the transfer learning of VGGNet even takes ~ 2 GPU hours.
- The handcrafted scattering networks provide a good level of discriminability here. However, it exhibits unsatisfactory scores for translation and rotation variants, even lower than the CNNs without augmentation, failing to achieve the expected robustness.
- The HIR significantly outperforms the main competitor, *i.e.*, scattering networks. It achieves a similar level of discriminability as the learning CNN family, also under the constraints of invariance and compactness. Note that our HIR is the only method exhibiting confusion between classes ‘6’ and ‘9’ in the direct training, while achieving $\sim 100\%$ scores for the rest. This phenomenon is in line with the rotation invariance and discriminative power expected by our theory.

4.2. Forensic Applications

For real-world applications, we employ the HIR for large-scale digital forensics, *i.e.*, detections of AIGC and adversarial perturbation, for direct checking its usefulness in robust and interpretable tasks. We have moved the applications on adversarial perturbations to [Section A8](#) due to space constraints. Note that this plug-and-play strategy will not only be compared to similar representations, but will also a range of current forensic solutions, including well-designed deep forensics.

The competing methods involved here can be summarized as follows:

Table 3. AIGC Forensic Scores (F1, %) for Different Representations *w.r.t.* Various Types of Generators.

Method	ADM	BGAN	GLIDE	Midj.	SD1.4	SD1.5	VQDM	Wukong	Avg	Min
<i>Classical:</i>										
Cosine NN	0.00	0.00	0.00	0.00	0.00	65.09	0.00	0.00	8.14	0.00
Cosine SVM	99.19	99.95	99.57	89.02	99.10	98.80	99.46	99.11	98.03	89.02
Wavelet NN	0.00	0.00	0.00	0.00	0.00	2.08	0.00	0.00	0.26	0.00
Wavelet SVM	99.98	99.70	99.87	85.55	98.63	99.04	99.97	99.38	97.76	85.55
Kraw. NN	0.00	0.00	0.00	0.00	0.00	0.00	0.00	0.00	0.00	0.00
Kraw. SVM	99.75	99.60	98.49	62.44	74.11	77.98	93.63	76.00	85.25	62.44
<i>Learning:</i>										
SimpleNet	98.25	97.87	92.98	68.00	73.52	74.37	74.88	76.32	82.02	68.00
AlexNet	94.45	98.99	98.26	81.52	87.96	88.66	84.24	88.62	90.34	81.52
VGGNet	99.40	99.38	98.57	86.44	89.97	91.86	93.60	90.09	93.66	86.44
GoogLeNet	80.30	99.18	98.16	75.00	82.77	82.44	86.75	82.32	85.87	75.00
ResNet	98.78	99.14	97.78	87.41	89.88	90.85	88.53	88.80	92.65	87.41
DenseNet	99.63	99.60	98.57	93.08	93.79	94.50	95.01	92.55	95.84	92.55
InceptionNet	97.69	99.41	98.32	90.07	89.40	92.55	92.72	88.35	93.96	88.35
MobileNet	90.08	99.28	97.95	87.49	88.51	90.75	87.74	88.29	91.26	87.49
<i>Invariant:</i>										
ScatterNet NN	99.10	99.63	98.44	79.47	89.26	89.95	96.71	89.07	92.70	79.47
ScatterNet SVM	99.18	99.67	99.05	85.21	95.85	95.58	97.02	94.60	95.77	85.21
HIR NN	99.92	99.97	99.83	92.63	98.57	98.97	99.92	98.58	98.55	92.63
HIR SVM	99.90	99.92	99.78	92.18	99.07	99.26	99.87	99.42	98.68	92.18

- All the representations in Section 4.1 as direct forensics;
- More deep representation milestones for direct forensics, *i.e.*, GoogLeNet [40], ResNet [15], DenseNet [16], InceptionNet [41], and MobileNet [35];
- The forensic methods designed for adversarial perturbation, *i.e.*, arXiv’17 [9], ICLR’18 [23], TDSC’18 [22], IJCV’19 [12], CVPR’19 [25], TDSC’20 [1], and arXiv’23 [44];
- The forensic methods designed for AIGC, *i.e.*, ECCV’20 [33], CVPR’20a [46], and CVPR’20b [26].

As shown in Fig. 5, fake images with similar content to ImageNet² are synthesized through 8 AIGC methods³, *i.e.*, ADM [8], BGAN [4], GLIDE [29], Midjourney⁴, SD 1.4 [34], SD 1.5 [34], VQDM [13], and Wukong⁵, respectively, resulting in 8 benchmarks, each containing 6000 natural images and 6000 synthesized images. This task exhibits higher level of discriminative challenges, in light of the very rich variability of both natural and synthesized content.

In Table 3, we train and test all representations on the 8 benchmarks, presenting the corresponding F1 scores, as well as the average and worst score statistics. Besides this direct protocol, we also consider testing image variants with random orientation or flipping in Table 4, reflecting the basic geometric robustness requirements.

- One can observe that the frequency forensic clue of the AI-generated pipeline is still very effective. The classical representations based on SVM classifier achieve consistently good accuracy and robustness, suggesting that state-of-the-art generators (even diffusion ones) still exhibit inherent frequency artifacts. However, such features exhibit significant sensitivity to classifiers. A potential reason is the restricted separability, where one must resort to complex classification strategies in the feature space.

²<https://www.image-net.org>

³<https://genimage-dataset.github.io>

⁴<https://www.midjourney.com/home>

⁵<https://xihe.mindspore.cn/modelzoo/wukong>

Table 4. AIGC forensic robustness scores (F1, %) for different representations *w.r.t.* various types of generators.

Method	Testing With Random Orientation and Flipping									
	ADM	BGAN	GLIDE	Midj.	SD1.4	SD1.5	VQDM	Wukong	Avg	Min
<i>Classical:</i>										
Cosine SVM	99.16	99.95	99.55	88.07	99.05	98.72	99.36	99.11	97.87	88.07
Wavelet SVM	99.95	99.80	99.85	82.83	99.08	98.71	99.95	99.16	97.42	82.83
Krawt. SVM	70.90	99.58	98.57	64.90	77.28	76.58	94.44	76.72	82.37	64.90
<i>Learning:</i>										
SimpleNet	77.72	95.04	92.99	65.25	74.52	74.72	73.62	76.91	78.85	65.25
AlexNet	81.82	99.08	97.99	77.45	85.87	87.93	83.29	86.78	87.53	77.45
VGGNet	76.18	99.40	98.41	82.23	89.26	89.30	88.79	89.00	89.07	76.18
GoogLeNet	80.62	99.30	98.09	73.13	81.29	81.92	85.36	82.31	85.25	73.13
ResNet	85.62	99.28	97.60	81.82	85.60	86.84	87.94	85.21	88.74	81.82
DenseNet	84.57	99.56	98.66	88.57	91.16	91.60	94.26	89.47	92.23	84.57
InceptionNet	91.99	99.30	98.56	87.04	85.72	88.85	92.19	85.24	91.11	85.24
MobileNet	85.14	99.36	97.78	84.54	86.74	88.80	87.50	86.56	89.55	84.54
<i>Invariant:</i>										
ScatterNet SVM	92.61	99.67	99.18	82.75	88.81	89.40	97.05	83.83	91.66	82.75
HIR SVM	99.88	99.87	99.77	91.99	99.02	99.25	99.83	99.45	98.63	91.99

- The learning representations other than SimpleNet and GoogLeNet achieve $> 90\%$ average scores, further confirming their good discriminability with sufficient training data and aligned testing protocol. However, for the robustness protocol in Table 4, they exhibit varying degrees of performance degradation, in both average and worst statistics. Clearly, even natural and slight shifts in the data distribution can strongly interfere with the learning forensics. In particular, such interference is highly black-boxed (*i.e.*, unpredictable), where an example is the significantly higher fluctuations on ADM compared to others.
- The scattering networks exhibit similar level of discriminability and robustness as the learning representations, while outperforming the original wavelets in classifier stability. Note that scattering networks fails to achieve the expected invariance and thus cannot provide higher robustness scores than learning CNNs.
- Regarding the discriminability, geometric invariance, and classifier stability, our HIR achieves better combined performance versus classical representations, scattering networks, and learning CNNs. This is in line with our theory expectation that HIR combines the advantages of both hand-crafted and learning representations. While its efficiency will be further highlighted in the next experimental protocol.

In Table 5, we train and test all representations on a hybrid of the 8 AIGC benchmarks, presenting scores at two training-testing ratios. This protocol is more challenging due to very complex intra-class variability, while being more practical for real-world forensic scenarios.

- The classical representations exhibit good discriminability for this hybrid benchmark, along with the benefit of sample efficiency. In line with previous observations, they still exhibit score fluctuations on the two classifiers.
- The forensic scores of the learning CNN family drop significantly, with average scores of only $\sim 70\%$ in the 1/9 case. This further illustrates the weakness of learning forensic algorithms in dealing with real-world scenarios, *i.e.*, the data dependence problem.

Table 5. AIGC forensic scores (%) for different representations on a real-world (hybrid) benchmark

Method	Train/Test. = 5/5			Train./Test. = 1/9		
	Pre.	Rec.	F1	Pre.	Rec.	F1
<i>Classical:</i>						
Cosine NN	0.00	0.00	0.00	0.00	0.00	0.00
Cosine SVM	94.95	94.57	94.76	94.36	91.06	92.68
Wavelet NN	48.70	94.17	64.20	48.69	94.13	64.18
Wavelet SVM	94.03	94.57	94.30	83.55	93.48	88.24
Kraw. NN	0.00	0.00	0.00	0.00	0.00	0.00
Kraw. SVM	75.24	74.77	75.00	71.56	68.57	70.03
<i>Learning:</i>						
SimpleNet	61.79	40.70	49.08	56.40	60.48	58.37
AlexNet	80.76	77.63	79.16	71.83	72.50	72.17
VGGNet	84.75	86.67	85.70	72.45	72.37	72.41
GoogLeNet	74.15	80.40	77.15	67.84	68.83	68.33
ResNet	85.10	83.03	84.06	76.88	73.67	75.24
DenseNet	86.83	85.23	86.02	76.84	75.37	76.10
InceptionNet	82.69	86.63	84.62	68.62	68.56	68.59
MobileNet	81.54	82.47	82.00	68.52	68.57	68.55
<i>Invariant:</i>						
Scatter. NN	83.68	83.73	83.71	79.37	79.70	79.53
Scatter. SVM	90.31	85.17	87.67	85.28	79.70	82.40
HIR NN	96.79	96.47	96.63	95.66	93.04	94.33
HIR SVM	96.92	96.37	96.64	95.21	94.26	94.73

- The scattering networks inherits the discriminability level and classifier stability from Table 4, also with better scores than all learning representations in the 1/9 case. These all indicate the superiority in combined performance.
- Here, the HIR achieves the highest scores over classical representations, scattering networks, and learning CNNs. Its discriminability allows for a hybrid forensic of the 8 AIGC methods in the 1/9 case with fewer samples, implying the usefulness in real-world forensic scenarios. Note that the ECCV'20, CVPR'20a, and CVPR'20b specifically designed for AIGC forensics exhibit 79.67%, 73.74%, and 76.89% F1 scores in the 1/9 case, respectively.

5. Conclusion

In this paper, we have systematically investigated the topic of hierarchical invariance, as an early attempt to harmonize the divergence between typical CNNs and invariants *w.r.t.* discriminability and robustness. Compared to related research approaches, our hierarchical invariant representation can be characterized as 1) principled and transparent design, 2) efficient invariant structure, and 3) competitive discriminability in the era of deep learning.

6. Acknowledgments

This work was supported in part by the Lagrange Mathematics and Computing Research Center of Huawei Technologies France, the Startup Fund of the City University of Hong Kong, the National Natural Science Foundation of China under Grants 62025604 and 62441619, and the Gansu Talent Program of Jiangxi Province under Grant gpyc20240012.

References

- [1] Akshay Agarwal, Richa Singh, Mayank Vatsa, and Nalini Ratha. Image transformation-based defense against adversarial perturbation on deep learning models. *IEEE Trans. Dependable Secure Comput.*, 18(5):2106–2121, 2020. 7
- [2] Gabriel Bender, Pieter-Jan Kindermans, Barret Zoph, Vijay Vasudevan, and Quoc Le. Understanding and simplifying one-shot architecture search. In *Proc. Int. Conf. Mach. Learn.*, pages 550–559, 2018. 6
- [3] Yoshua Bengio, Aaron Courville, and Pascal Vincent. Representation learning: A review and new perspectives. *IEEE Trans. Pattern Anal. Mach. Intell.*, 35(8):1798–1828, 2013. 1
- [4] Andrew Brock, Jeff Donahue, and Karen Simonyan. Large scale GAN training for high fidelity natural image synthesis. *arXiv preprint arXiv:1809.11096*, 2018. 7
- [5] Michael M Bronstein, Joan Bruna, Taco Cohen, and Petar Veličković. Geometric deep learning: Grids, groups, graphs, geodesics, and gauges. *arXiv preprint arXiv:2104.13478*, 2021. 1
- [6] Joan Bruna and Stéphane Mallat. Invariant scattering convolution networks. *IEEE Trans. Pattern Anal. Mach. Intell.*, 35(8):1872–1886, 2013. 2, 6
- [7] Taco Cohen and Max Welling. Group equivariant convolutional networks. In *Proc. Int. Conf. Mach. Learn.*, pages 2990–2999, 2016. 2
- [8] Prafulla Dhariwal and Alexander Nichol. Diffusion models beat GANs on image synthesis. *Proc. Adv. Neural Inf. Process. Syst.*, 34:8780–8794, 2021. 7
- [9] Reuben Feinman, Ryan R Curtin, Saurabh Shintre, and Andrew B Gardner. Detecting adversarial samples from artifacts. *arXiv preprint arXiv:1703.00410*, 2017. 7
- [10] Shuo Feng, Haowei Sun, Xintao Yan, Haojie Zhu, Zhengxia Zou, Shengyin Shen, and Henry X Liu. Dense reinforcement learning for safety validation of autonomous vehicles. *Nature*, 615(7953):620–627, 2023. 1
- [11] Kunihiko Fukushima and Sei Miyake. Neocognitron: A new algorithm for pattern recognition tolerant of deformations and shifts in position. *Pattern Recognit.*, 15(6):455–469, 1982. 1
- [12] Gaurav Goswami, Akshay Agarwal, Nalini Ratha, Richa Singh, and Mayank Vatsa. Detecting and mitigating adversarial perturbations for robust face recognition. *Int. J. Comput. Vis.*, 127:719–742, 2019. 7
- [13] Shuyang Gu, Dong Chen, Jianmin Bao, Fang Wen, Bo Zhang, Dongdong Chen, Lu Yuan, and Baining Guo. Vector quantized diffusion model for text-to-image synthesis. In *Proc. IEEE Conf. Comput. Vis. Pattern Recognit.*, pages 10696–10706, 2022. 7
- [14] Minghao Guo, Yuzhe Yang, Rui Xu, Ziwei Liu, and Dahua Lin. When NAS meets robustness: In search of robust architectures against adversarial attacks. In *Proc. IEEE Conf. Comput. Vis. Pattern Recognit.*, pages 631–640, 2020. 6
- [15] Kaiming He, Xiangyu Zhang, Shaoqing Ren, and Jian Sun. Deep residual learning for image recognition. In *Proc. IEEE Conf. Comput. Vis. Pattern Recognit.*, pages 770–778, 2016. 7
- [16] Gao Huang, Zhuang Liu, Laurens Van Der Maaten, and Kilian Q Weinberger. Densely connected convolutional networks. In *Proc. IEEE Conf. Comput. Vis. Pattern Recognit.*, pages 4700–4708, 2017. 7
- [17] Felix Juefei-Xu, Run Wang, Yihao Huang, Qing Guo, Lei Ma, and Yang Liu. Counteracting malicious deepfakes: Survey, battleground, and horizon. *Int. J. Comput. Vis.*, 130(7):1678–1734, 2022. 1
- [18] Felix Klein. A comparative review of recent researches in geometry. *Bull. Am. Math. Soc.*, 2(10):215–249, 1893. 1
- [19] Alex Krizhevsky, Ilya Sutskever, and Geoffrey E Hinton. ImageNet classification with deep convolutional neural networks. *Commun. ACM*, 60(6):84–90, 2017. 6
- [20] Yann LeCun, Yoshua Bengio, and Geoffrey Hinton. Deep learning. *Nature*, 521(7553):436–444, 2015. 1
- [21] Karel Lenc and Andrea Vedaldi. Understanding image representations by measuring their equivariance and equivalence. In *Proc. IEEE Conf. Comput. Vis. Pattern Recognit.*, pages 991–999, 2015. 3
- [22] Bin Liang, Hongcheng Li, Miaoqiang Su, Xirong Li, Wenchang Shi, and Xiaofeng Wang. Detecting adversarial image examples in deep neural networks with adaptive noise reduction. *IEEE Trans. Dependable Secure Comput.*, 18(1):72–85, 2018. 7
- [23] Shiyu Liang, Yixuan Li, and R Srikant. Enhancing the reliability of out-of-distribution image detection in neural networks. In *Proc. Int. Conf. Learn. Representations*, 2018. 7
- [24] Haoyang Liu, Maheep Chaudhary, and Haohan Wang. Towards trustworthy and aligned machine learning: A data-centric survey with causality perspectives. *arXiv preprint arXiv:2307.16851*, 2023. 1
- [25] Jiayang Liu, Weiming Zhang, Yiwei Zhang, Dongdong Hou, Yujia Liu, Hongyue Zha, and Nenghai Yu. Detection based defense against adversarial examples from the steganalysis point of view. In *Proc. IEEE Conf. Comput. Vis. Pattern Recognit.*, pages 4825–4834, 2019. 7
- [26] Zhengze Liu, Xiaojuan Qi, and Philip HS Torr. Global texture enhancement for fake face detection in the wild. In *Proc. IEEE Conf. Comput. Vis. Pattern Recognit.*, pages 8060–8069, 2020. 7
- [27] Stephane G Mallat. A theory for multiresolution signal decomposition: The wavelet representation. *IEEE Trans. Pattern Anal. Mach. Intell.*, 11(7):674–693, 1989. 6
- [28] Diego Marcos, Michele Volpi, Nikos Komodakis, and Devis Tuia. Rotation equivariant vector field networks. In *Proc. IEEE Int. Conf. Comput. Vis.*, pages 5048–5057, 2017. 3
- [29] Alex Nichol, Prafulla Dhariwal, Aditya Ramesh, Pranav Shyam, Pamela Mishkin, Bob McGrew, Ilya Sutskever, and Mark Chen. Glide: Towards photorealistic image generation and editing with text-guided diffusion models. *arXiv preprint arXiv:2112.10741*, 2021. 7
- [30] Edouard Oyallon, Sergey Zagoruyko, Gabriel Huang, Nikos Komodakis, Simon Lacoste-Julien, Matthew Blaschko, and Eugene Belilovsky. Scattering networks for hybrid representation learning. *IEEE Trans. Pattern Anal. Mach. Intell.*, 41(9):2208–2221, 2018. 6

- [31] Shuren Qi, Yushu Zhang, Chao Wang, Jiantao Zhou, and Xiaochun Cao. A survey of orthogonal moments for image representation: theory, implementation, and evaluation. *ACM Comput. Surv.*, 55(1):1–35, 2021. [1](#), [2](#), [3](#), [4](#)
- [32] Shuren Qi, Yushu Zhang, Chao Wang, Jiantao Zhou, and Xiaochun Cao. A principled design of image representation: Towards forensic tasks. *IEEE Trans. Pattern Anal. Mach. Intell.*, 45(5):5337–5354, 2022. [3](#)
- [33] Yuyang Qian, Guojun Yin, Lu Sheng, Zixuan Chen, and Jing Shao. Thinking in frequency: Face forgery detection by mining frequency-aware clues. In *Proc. Eur. Conf. Comput. Vis.*, pages 86–103, 2020. [7](#)
- [34] Robin Rombach, Andreas Blattmann, Dominik Lorenz, Patrick Esser, and Björn Ommer. High-resolution image synthesis with latent diffusion models. In *Proc. IEEE Conf. Comput. Vis. Pattern Recognit.*, pages 10684–10695, 2022. [7](#)
- [35] Mark Sandler, Andrew Howard, Menglong Zhu, Andrey Zhmoginov, and Liang-Chieh Chen. Mobilenet-v2: Inverted residuals and linear bottlenecks. In *Proc. IEEE Conf. Comput. Vis. Pattern Recognit.*, pages 4510–4520, 2018. [7](#)
- [36] David Silver, Julian Schrittwieser, Karen Simonyan, Ioannis Antonoglou, Aja Huang, Arthur Guez, Thomas Hubert, Lucas Baker, Matthew Lai, Adrian Bolton, et al. Mastering the game of go without human knowledge. *Nature*, 550(7676):354–359, 2017. [1](#)
- [37] Karen Simonyan and Andrew Zisserman. Very deep convolutional networks for large-scale image recognition. *arXiv preprint arXiv:1409.1556*, 2014. [6](#)
- [38] Zikai Sun and Thierry Blu. Empowering networks with scale and rotation equivariance using a similarity convolution. In *Proc. Int. Conf. Learn. Representations*, 2023. [2](#)
- [39] Kalaivani Sundararajan and Damon L Woodard. Deep learning for biometrics: A survey. *ACM Comput. Surv.*, 51(3):1–34, 2018. [1](#)
- [40] Christian Szegedy, Wei Liu, Yangqing Jia, Pierre Sermanet, Scott Reed, Dragomir Anguelov, Dumitru Erhan, Vincent Vanhoucke, and Andrew Rabinovich. Going deeper with convolutions. In *Proc. IEEE Conf. Comput. Vis. Pattern Recognit.*, pages 1–9, 2015. [7](#)
- [41] Christian Szegedy, Vincent Vanhoucke, Sergey Ioffe, Jon Shlens, and Zbigniew Wojna. Rethinking the inception architecture for computer vision. In *Proc. IEEE Conf. Comput. Vis. Pattern Recognit.*, pages 2818–2826, 2016. [7](#)
- [42] Renate Tobies. *Felix Klein—Mathematician, Academic Organizer, Educational Reformer*, pages 5–21. Springer International Publishing, Cham, 2019. [1](#)
- [43] Dmitry Ulyanov, Andrea Vedaldi, and Victor Lempitsky. Deep image prior. In *Proc. IEEE Conf. Comput. Vis. Pattern Recognit.*, pages 9446–9454, 2018. [1](#)
- [44] Chao Wang, Shuren Qi, Zhiqiu Huang, Yushu Zhang, Rushi Lan, and Xiaochun Cao. Towards an accurate and secure detector against adversarial perturbations. *arXiv preprint arXiv:2305.10856*, 2023. [7](#)
- [45] Hanchen Wang, Tianfan Fu, Yuanqi Du, Wenhao Gao, Kexin Huang, Ziming Liu, Payal Chandak, Shengchao Liu, Peter Van Katwyk, Andreea Deac, et al. Scientific discovery in the age of artificial intelligence. *Nature*, 620(7972):47–60, 2023. [1](#)
- [46] Sheng-Yu Wang, Oliver Wang, Richard Zhang, Andrew Owens, and Alexei A Efros. CNN-generated images are surprisingly easy to spot... for now. In *Proc. IEEE Conf. Comput. Vis. Pattern Recognit.*, pages 8695–8704, 2020. [7](#)
- [47] Stefanie Warnat-Herresthal, Hartmut Schultze, Krishnaprasad Lingadahalli Shastry, Sathyanarayanan Manamohan, Saikat Mukherjee, Vishesh Garg, Ravi Sarveswara, Kristian Händler, Peter Pickkers, N Ahmad Aziz, et al. Swarm learning for decentralized and confidential clinical machine learning. *Nature*, 594(7862):265–270, 2021. [1](#)
- [48] Jeannette M Wing. Trustworthy AI. *Commun. ACM*, 64(10):64–71, 2021. [1](#)
- [49] P-T Yap, Raveendran Paramesran, and Seng-Huat Ong. Image analysis by Krawtchouk moments. *IEEE Trans. Image Process.*, 12(11):1367–1377, 2003. [6](#)
- [50] Richard Zhang. Making convolutional networks shift-invariant again. In *Proc. Int. Conf. Mach. Learn.*, pages 7324–7334, 2019. [1](#), [2](#), [4](#)

Appendix for “Transparent Vision: A Theory of Hierarchical Invariant Representations”

A1. Historical Perspectives of Invariance

We provide some historical perspectives on the invariance in the development of image representations. The quest for invariance dates back to the gestation of computer vision itself, spanning both hand-crafted and learning approaches [3]:

- In the hand-crafted approach, symmetry priors (*e.g.*, invariance and equivariance) *w.r.t.* geometric transformations (*e.g.*, translation, rotation, and scaling) have been recognized as main ideas in designing representations. Such ideas cover almost all classical and state-of-the-art methods, from global features (*e.g.*, moment invariants [25]), to local sparse features (*e.g.*, SIFT [20]), and to local dense features (*e.g.*, DAISY [33]). However, these hand-crafted representations are all fixed in design, relying on (*under*)-*complete* dictionaries, and therefore fail to provide sufficient discriminability at larger scales, *e.g.*, ImageNet classification task [28].
- In the learning approach, CNNs achieve *over-complete* representations of strong discriminative power for larger-scale vision tasks, through a cascade of learnable nonlinear transformations. As a textbook view of deep learning, representations should be learned not designed [18]. Therefore, typical CNN representations are equipped with very few symmetry priors, typically just translation equivariance [15], but has recently been proven to no longer hold in deeper layers of the CNNs with down-sampling structures [42]. In general, these learning representations lack robustness and interpretability guarantees, *e.g.*, the presence and understanding of adversarial perturbations [6], and therefore cannot be well extended to trustworthy tasks [32].

Historically, to a certain extent, efforts at invariance and discriminability have developed independently in hand-crafted and learning approaches. The compatibility between invariance and discriminability has emerged as a tricky problem when moving towards trustworthy AI.

A2. Related Works

In this section, we supplement the developmental efforts of scattering and equivariant networks.

A2.1. Scattering Networks

Theoretical works further explored various geometric invariants [29], more general mathematical formulations [36], and the potential for improving the efficiency, interpretability, and robustness of state-of-the-art CNN techniques [24]. Regarding applications, they provided competitive results in a variety of tasks on audio [1], image [5, 24, 29] and graph [9] data, some of which are even interdisciplinary [10, 41].

A2.2. Equivariant Networks

Theoretical works further explored the equivariance for rotation [12, 35, 38], flipping [12], scaling [30, 37], and their combination [31] from various mathematical theories, including steerable filters [12], harmonic analysis [38], scale space [37], Lie groups [13], and B-spline interpolation [4]. Regarding applications, they played a key role in low-level vision tasks [39], especially scientific discoveries with symmetry priors [2, 34].

A3. Foundations of Invariant Theory

Our work develops from the theory of moment invariants. Therefore, we begin with a brief review on the foundations of moment invariants, covering some concepts, notations, and definitions.

A3.1. Global and Local Representations

In general, classical moments and moment invariants are *global* representations of images, where the theory is built on the following definition [25]:

$$\langle f, V_{nm} \rangle = \iint_D V_{nm}^*(x, y) f(x, y) dx dy, \quad (\text{A1})$$

where f is the image function, V_{nm} is the basis function with order parameter $(n, m) \in \mathbb{Z}^2$ on domain D , and $*$ is the complex conjugate. Note that the domains of f and V_{nm} in (A1) have the same/similar location and scale, implying the global nature of the representation information.

With the sparse prior and geometric prior for natural images, two typical constraints, *i.e.*, orthogonality and rotation invariance, often imposed on the explicit definition of V_{nm} ,

leading to the following polar form:

$$\langle f, V_{nm} \rangle = \iint_D R_n^*(r) A_m^*(\theta) f(r, \theta) r dr d\theta, \quad (\text{A2})$$

where $V_{nm}(r \cos \theta, r \sin \theta) \equiv V_{nm}(r, \theta)$ is separated as the product of the angular basis function $A_m(\theta) = \exp(jm\theta)$ ($j = \sqrt{-1}$) and the radial basis function R_n , subject to the weighted orthogonality condition $\int_0^1 R_n(r) R_{n'}^*(r) r dr = \frac{1}{2\pi} \delta_{nn'}$. Note that the basis function $V_{nm} = R_n A_m$ in (A2) is orthogonal on D , and the magnitude of $\langle f, V_{nm} \rangle$ is invariant to the rotation on the image f (see [25] for a survey).

In our recent work, moments and moment invariants are extended to *local* representations of images, where the theory is built on the following definition [26]:

$$\langle f, V_{nm}^{uvw} \rangle = \iint_D R_n^*(r') A_m^*(\theta') f(x, y) dx dy, \quad (\text{A3})$$

where the new basis function V_{nm}^{uvw} introduces position parameters (u, v) and scale parameter w . It can be interpreted as a translated and scaled version of the global V_{nm} with the following coordinate relationship:

$$\begin{cases} r' = \frac{1}{w} \sqrt{(x - u)^2 + (y - v)^2} \\ \theta' = \arctan\left(\frac{y - v}{x - u}\right) \end{cases}, \quad (\text{A4})$$

where the domain is a disk centered at (u, v) and with radius w : $D = \{(x, y) : (x - u)^2 + (y - v)^2 \leq w^2\}$. Note that (A3) allows the domain of V_{nm}^{uvw} to be built in different positions and scales *w.r.t.* the domain of f , implying the local nature of the representation information. Also, the classical definition (A2) is in fact a special case of the new definition (A3) with $(u, v) = (0, 0)$ and $w = 1$ (see [26] for details).

A3.2. Invariance, Equivariance, and Covariance

The terms of invariance, equivariance, and covariance appear in the fields of computer vision, graphics, geometry, and physics. We use the following identities to generally denote such terms [19, 22]:

- invariance — $\mathcal{R}(\mathcal{D}(f)) \equiv \mathcal{R}(f)$,
- equivariance — $\mathcal{R}(\mathcal{D}(f)) \equiv \mathcal{D}(\mathcal{R}(f))$,
- covariance — $\mathcal{R}(\mathcal{D}(f)) \equiv \mathcal{D}'(\mathcal{R}(f))$,

where \mathcal{R} is a representation, \mathcal{D} is a degradation, and \mathcal{D}' is a composite function of \mathcal{D} . Note that invariance and equivariance are special cases of covariance with $\mathcal{D}' = \text{id}$ and $\mathcal{D}' = \mathcal{D}$.

Starting from the local representation (A3), one can verify that $\langle f, V_{nm}^{uvw} \rangle$ exhibits the following properties *w.r.t.* translation, rotation, flipping, and scaling on images (see [26] for details).

The image *translation* leads to

$$\begin{aligned} & \langle f(x + \Delta x, y + \Delta y), V_{nm}^{uvw}(x, y) \rangle \\ &= \langle f(x, y), V_{nm}^{(u+\Delta x)(v+\Delta y)w}(x, y) \rangle, \end{aligned} \quad (\text{A5})$$

where $(\Delta x, \Delta y)$ is the translation offset of the image f . Note that the same $(\Delta x, \Delta y)$ appears in position parameters (u, v) , implying the equivariance *w.r.t.* the image translation.

Since the translation equivariance holds, the following analysis (A6) ~ (A8) will consider only center-aligned geometric transformations, *i.e.*, we can restrict $(u, v) = (0, 0)$ without loss of generality.

The image *rotation* leads to

$$\begin{aligned} & \langle f(r, \theta + \phi), V_{nm}^{uvw}(r', \theta') \rangle \\ &= \langle f(r, \theta), V_{nm}^{uvw}(r', \theta') \rangle A_m^*(-\phi), \end{aligned} \quad (\text{A6})$$

with $(u, v) = (0, 0)$, where ϕ is the rotation angle *w.r.t.* the center of the image f . Note that the same ϕ appears in the phase of the representation, implying the covariance *w.r.t.* the center-aligned rotation. It is straightforward that the covariance (A3) will specialize to the invariance when taking the magnitude as $|\langle f(r, \theta + \phi), V_{nm}^{uvw}(r', \theta') \rangle| = |\langle f(r, \theta), V_{nm}^{uvw}(r', \theta') \rangle|$.

The image *flipping* leads to

$$\begin{aligned} & \langle f(r, -\theta), V_{nm}^{uvw}(r', \theta') \rangle \\ &= (\langle f(r, \theta), V_{nm}^{uvw}(r', \theta') \rangle)^*, \end{aligned} \quad (\text{A7})$$

with $(u, v) = (0, 0)$, where $f(r, -\theta)$ is a vertically flipped version of the image f *w.r.t.* the center. Note that center-aligned vertical flipping again only affects the phase of the representation, implying the covariance similar to (A6). As for other flipping orientations, the same conclusion can be derived from the composite of rotation and vertical flipping. It is straightforward that the joint invariance of center-aligned rotation and flipping holds when taking the magnitude of the representation.

The image *scaling* leads to

$$\begin{aligned} & \langle f(sx, sy), V_{nm}^{uvw}(x, y) \rangle \\ &= \langle f(x, y), V_{nm}^{uv(ws)}(x, y) \rangle, \end{aligned} \quad (\text{A8})$$

with $(u, v) = (0, 0)$, where s is the scaling factor *w.r.t.* the center of the image f . Note that the same s appears in the scale parameter w , implying the covariance *w.r.t.* center-aligned scaling.

For the representation properties when $(u, v) \neq (0, 0)$, they can be derived from the composite of translation with center-aligned rotation, flipping, and scaling, respectively. Hence, the magnitude of the representation has *joint equivariance for any translation, rotation, and flipping* on (u, v) domain, as well as *covariance for any scaling* on w domain.

A4. Proofs

A4.1. Equivariance Properties

Proof. First, let us examine the behavior of a representation unit \mathbb{U} on \mathfrak{G}_1 :

$$\begin{aligned}\mathbb{U}(\mathfrak{g}_1 M) &= \mathbb{P} \circ \mathbb{S} \circ \mathbb{C}(\mathfrak{g}_1 M) \\ &= \mathbb{P} \circ \mathbb{S} \circ \mathfrak{g}'_1 \mathbb{C}(M) \\ &= \mathbb{P} \circ \mathfrak{g}_1 \mathbb{S} \circ \mathbb{C}(M) \\ &= \mathfrak{g}_1 \mathbb{P} \circ \mathbb{S} \circ \mathbb{C}(M) \\ &= \mathfrak{g}_1 \mathbb{U}(M),\end{aligned}\tag{A9}$$

where the first pass comes from the covariance of \mathbb{C} for rotation and flipping, *i.e.*, (A6) and (A7), and \mathfrak{g}'_1 is a predictable operation acting in the phase domain of $\mathbb{C}(M)$; the second pass comes from the specialization of \mathbb{S} to the covariant \mathfrak{g}'_1 – the magnitude operation removes the extra phase variations, leading to a pure equivariance \mathfrak{g}_1 ; the third pass comes from the identity function of \mathbb{P} , which becomes approximately equal when the downsampled \mathbb{P} is used.

Here, $\mathbb{U}(\mathfrak{g}_1 M) = \mathfrak{g}_1 \mathbb{U}(M)$ means that the representation unit \mathbb{U} can be considered as an *equivariant layer* for any $\mathfrak{g}_1 \in \mathfrak{G}_1$ and $M \in X$ – in other words, the single \mathbb{U} and \mathfrak{g}_1 operations on $M \in X$ are *exchangeable*. Furthermore, with a notation $M_{[l]} \triangleq \mathbb{U}_{[l]} \circ \dots \circ \mathbb{U}_{[1]}(M) = \mathbb{U}_{[l]} M_{[l-1]}$, we have $M_{[l]} \in X$ for any $l \in \{1, 2, \dots, L\}$. Therefore, \mathfrak{g}_1 and any composition of \mathbb{U} are exchangeable, implying the correctness of Property 1. \square

A4.2. Covariance Properties

Proof. First, let us examine the behavior of a representation unit \mathbb{U}^w on \mathfrak{G}_2 :

$$\begin{aligned}\mathbb{U}^w(\mathfrak{g}_2 M) &= \mathbb{P} \circ \mathbb{S} \circ \mathbb{C}^w(\mathfrak{g}_2 M) \\ &= \mathbb{P} \circ \mathbb{S} \circ \mathfrak{g}'_2 \mathbb{C}^w(M) \\ &= \mathbb{P} \circ \mathbb{S} \circ \mathfrak{g}_2 \mathbb{C}^{ws}(M) \\ &= \mathbb{P} \circ \mathfrak{g}_2 \mathbb{S} \circ \mathbb{C}^{ws}(M) \\ &= \mathfrak{g}_2 \mathbb{P} \circ \mathbb{S} \circ \mathbb{C}^{ws}(M) \\ &= \mathfrak{g}_2 \mathbb{U}^{ws}(M) \\ &= \mathfrak{g}'_2 \mathbb{U}^w(M),\end{aligned}\tag{A10}$$

where the first pass comes from the covariance of \mathbb{C} for scaling, *i.e.*, (A8), and \mathfrak{g}'_2 is a predictable operation acting in both the Ω domain (*i.e.*, the same scaling \mathfrak{g}_2) and the w domain (*i.e.*, the factor s) of $\mathbb{C}^w(M)$; the second and third passes come from the element-wise act of \mathbb{S} and the identity function of \mathbb{P} , respectively.

Here, $\mathbb{U}^w(\mathfrak{g}_2 M) = \mathfrak{g}'_2 \mathbb{U}^w(M)$ means that the representation unit \mathbb{U}^w can be considered as an *covariant layer* for any $\mathfrak{g}_2 \in \mathfrak{G}_2$ and $M \in X$ – in other words, the single \mathbb{U}^w and \mathfrak{g}_2 operations on $M \in X$ are *exchangeable but with the parameter changing of ws*. Furthermore, we have

$M_{[l]} \in X$ for any $l \in \{1, 2, \dots, L\}$. Therefore, \mathfrak{g}_2 and any composition of \mathbb{U}^w are exchangeable while changing the scale parameter to ws , implying the correctness of Property 2. \square

A4.3. Invariance Properties

Proof. We can rewrite $\mathbb{I}(\mathfrak{g}'_0 M)_{[L]}$ as:

$$\begin{aligned}\mathbb{I}(\mathfrak{g}_0 M)_{[L]} &= \mathbb{I} \circ \mathbb{U}_{[L]} \circ \dots \circ \mathbb{U}_{[2]} \circ \mathbb{U}_{[1]}(\mathfrak{g}_0 M) \\ &= \mathbb{I}(\mathfrak{g}'_0 \mathbb{U}_{[L]} \circ \dots \circ \mathbb{U}_{[2]} \circ \mathbb{U}_{[1]}(M)) \\ &= \mathbb{I} \circ \mathbb{U}_{[L]} \circ \dots \circ \mathbb{U}_{[2]} \circ \mathbb{U}_{[1]}(M) \\ &= \mathbb{I} M_{[L]},\end{aligned}\tag{A11}$$

where the first pass comes from Properties 1 and 2, note that $\mathfrak{g}_0 \in \mathfrak{G}_0 \subseteq \mathfrak{G}_1 \times \mathfrak{G}_2$, \mathfrak{g}'_0 is related to \mathfrak{g}_1 and \mathfrak{g}'_2 ; the second pass comes from our assumption $\mathbb{I}(\mathfrak{g}'_0 M) = \mathbb{I}(M)$ for any $\mathfrak{g}_0 \in \mathfrak{G}_0$ and $M \in X$, with $M_{[l]} \in X$ for any $l \in \{1, 2, \dots, L\}$. Therefore, $\mathbb{I}(\mathfrak{g}'_0 M)_{[L]} \equiv \mathbb{I} M_{[L]}$, implying the correctness of Property 3. \square

A5. Theoretical Comparisons

It is necessary to highlight the theoretical relationships with typical related works:

- **Traditional Invariants:** Our work generalizes this theory by unifying the global and local invariant representations into a new framework of HIR. More specifically, we formalize layers \mathbb{C} , \mathbb{S} , and \mathbb{P} based on the theory of local invariants [26] (Definitions 1 ~ 3), arguing the equivariance/covariance can be preserved across layers under a certain cascade (Properties 1 ~ 2). We also formalize layer \mathbb{I} based on the theory of global invariants [25] (Definition 4), arguing the successes of global invariance for image domains can be directly generalized to equivariant/covariant deep feature domains (Property 3). Under our hierarchical invariance, classical global [25] and local [26] invariants can be considered as special cases, *i.e.*, $\mathbb{I}f$ and $\mathbb{I} \circ \mathbb{S} \circ \mathbb{C}f$ (Definition 5).
- **Traditional CNNs:** Our work has a similar hierarchical architecture but with better properties in geometric symmetry, allowing for robust and interpretable image representations. More specifically, we introduce the discriminative design of CNNs in our invariants, *i.e.*, over-complete representation with deep cascading [42]. On the other hand, we criticize typical CNN modules (Formulation 1), allowing fully transparent geometric symmetries across layers of our representation (Properties 1 ~ 3). As a result, the proposed representation serves as an effective alternative to the highly black-box CNNs in trustworthy tasks.
- **Scattering Networks:** Our work is more compact in achieving rotation invariance. As a main competitor, scattering networks are also based on deep cascading of

explicit transforms (wavelets) [5], with similar concepts to our work. However, constructing rotation invariants from scattering networks is complicated, which requires parallel convolution and cross-channel pooling of multiple oriented wavelets; increasing the orientation sampling will result in an exponential growth of the complexity. Whereas our approach benefits from classical invariant theory, rotation invariance is continuous and one-shot (Property 1), providing better efficiency while easily enlarging the network size to improve the representation capacity.

- **Equivariant Networks:** Our work is non-learning while being more compact in achieving continuous and joint invariance. As a secondary competitor, equivariant networks are also guaranteed by group theory [11], with similar concepts to our work. However, the convolutional layers in equivariant networks are learned, leading to varying degrees of data dependence. In particular, it has a similar parallel structure to scattering networks, leading to exponential complexity and optimization challenges. Although equivariant networks are a very generic design, our approach provides better efficiency for continuous and joint invariance (Properties 1 ∼ 3), while easily enlarging the network size to improve the representation capacity.

A6. Practical Details

In this section, we discuss more practical details on numerical implementations, network parameters, layer settings.

A6.1. Fast and Accurate Implementation

We will complement the numerical implementation of HIR, especially the fast and accurate computations of Definition 1 from our previous work [26]. Note that the discussion here is very general, with no restrictions on the specific definitions of the basis functions.

Definition (Fast Implementation). *Let us introduce the convolution theorem as a fast implementation of Definition 1, such that the spatial domain convolution of (A9) can be converted to the following frequency domain product form [26]:*

$$\mathbb{C}M = \mathcal{F}^{-1}(\mathcal{F}(M(i, j; k)) \odot \mathcal{F}((H_{nm}^w(i, j))^T)), \quad (\text{A12})$$

where \mathcal{F} is the Fourier transform and \odot is the point-wise multiplication.

Property (Complexity Analysis). *In Definition 1, the (1) dominates the computational complexity due to the dense convolution. For the input feature map $M(i, j; k)$ with $\Omega = \{1, 2, \dots, N_i\} \times \{1, 2, \dots, N_j\}$ and $H = \mathfrak{C}^K$, we assume that a set of $\mathbb{C}M$ needs to be computed, where the scale parameter $w \in S_w$ with a fixed order (n, m) and*

a fixed channel k , and denote the number of feature map samples as $N_{ij} = N_i N_j$ and the number of scale samples as $N_w = |S_w|$. With the above definition and the Fast Fourier Transform (FFT), we can compute the set of $\mathbb{C}M$ in $\mathcal{O}(N_w N_{ij} \log N_{ij})$ multiplications, as opposed to the complexity of $\mathcal{O}(N_w N_{ij} w_{\max}^2)$ by the direct Definition 1, where w_{\max} is the maximum scale in S_w . Note that the big difference between square and logarithmic growths in the complexity (removing the same terms), where the above definition will exhibit better efficiency when w_{\max} is sufficiently large such that $w_{\max}^2 > \log N_{ij}$.

Definition (Accurate Implementation). *Let us introduce the higher-order numerical integration as an accurate implementation of Definition 1, such that the two-dimensional continuous integral of (3) can be converted to the following summation form [26]:*

$$h_{nm}^{uvw}(i, j) \simeq \sum_{(a, b) \in S_{ab}} c_{ab} (V_{nm}^{uvw}(x_a, y_b))^* \frac{\Delta i \Delta j}{w^2}, \quad (\text{A13})$$

where the set of numerical integration samples S_{ab} encodes the points $(x_a, y_b) \in D_{ij}$ and the corresponding weights c_{ab} , which are specified by a certain numerical integration strategy, such as Gaussian quadrature.

Property (Accurate Analysis). *In Definition 1, (3) dominates the computational accuracy due to the continuous integration of complicated functions. We assume that h_{nm}^{uvw} with a fixed order (n, m) and position (u, v) needs to be computed, and denote the number of numerical integration samples as $N_{ab} = |S_{ab}|$. The implementation based on the above definition exhibits an approximation error of $\mathcal{O}((\frac{\Delta i \Delta j}{w^2})^{N_{ab}+1})$. Note that when there is more than one sample within each pixel region, i.e., $N_{ab} > 1$, the above definition will exhibit better accuracy than the error of $\mathcal{O}((\frac{\Delta i \Delta j}{w^2})^2)$ by the direct Definition 1 (zero-order approximation).*

A6.2. Parameters of Single-scale Networks

Here, the order parameter (n, m) of the previous unit (blue) is always smaller than that of the subsequent ones (under a specific norm), so that the path exhibits an increasing trend in the order. With this design, the main information can be passed through the early nodes, and hence the subsequent nodes capture rich features. Also, the identity function (black) is introduced as a skip-connection trick, allowing the information to be passed to deeper nodes. In this paper, all units from the same level l are specified separately from the set $\{(n, m) : n + m = l, (n, m) \in \mathbb{N}^2\}$, i.e., their orders are equal under the ℓ_1 norm.

A6.3. Radial Basis Functions

In our previous work [27], two generic classes of radial basis functions have been introduced, based on a family of

harmonic functions:

$$R_n(\alpha, r) = \sqrt{\frac{\alpha r^{\alpha-2}}{2\pi}} \exp(j2n\pi r^\alpha), \quad (\text{A14})$$

and a family of polynomial functions:

$$\begin{aligned} R_n^\alpha(p, q, r) &= \sqrt{\frac{\alpha r^{\alpha q-2}(1-r^\alpha)^{p-q}(p+2n)\Gamma(q+n)n!}{2\pi\Gamma(p+n)\Gamma(p-q+n+1)}} \\ &\times \sum_{k=0}^n \frac{(-1)^k \Gamma(p+n+k)r^{\alpha k}}{k!(n-k)!\Gamma(q+k)}, \end{aligned} \quad (\text{A15})$$

respectively, where the fractional parameter $\alpha \in \mathbb{R}^+$, the polynomial parameters $p, q \in \mathbb{R}$ must fulfill $p - q > -1$ and $q > 0$. Both classes of functions can be used to define R_n in the (A2), satisfying the orthogonality condition.

For the sake of simplicity, a family of cosine functions are chosen in all experiments and applications, as a special case of the (A14):

$$R_n(r) = \begin{cases} \frac{1}{\sqrt{\pi}} & n = 0 \\ \sqrt{\frac{2}{\pi}} \cos(n\pi r^2) & n > 0 \end{cases}, \quad (\text{A16})$$

i.e., forming a hierarchical invariant version of the Polar Cosine Transform (PCT) [40]. Note that we try to show the superiority of the hierarchical invariant framework itself, even if relying on naive (A16).

A6.4. Invariant Layer

In the monograph [14] and our previous work [25], a number of strategies for directly constructing global invariants in image domains have been presented. They can be naturally used to define \mathcal{I} in (6), with the equivariant or covariant behavior of deep feature maps (Properties 1 ~ 3). In all experiments and applications of this paper, a class of global invariants is concisely designed based on frequency pooling.

Regarding (6), we first let the Fourier basis be $V_{nm}(x_i, y_j)$. Note that the Fourier Transform (FT) is highly understood in the signal processing community and can be considered a good foundation for interpretability. Then, based on the order/frequency sampling of the FT $(n, m) \in [-K, K]^2$, we define \mathcal{I} as a frequency-band integral in the polar system:

$$\begin{aligned} \mathcal{I}(\{\langle M, V_{nm} \rangle\}) &\triangleq \\ \{I_i = \sum_{(n,m) \in \mathcal{B}_i} \{|\langle M, V_{nm} \rangle|\} : i = 1, 2, \dots, \#_B\}, \end{aligned} \quad (\text{A17})$$

where $\mathcal{B}_i = \{(n, m) : \sqrt{2}K(i-1)/\#_B \leq \|(n, m)\|_2 \leq \sqrt{2}Ki/\#_B\}$ is the i -th frequency band under the ℓ_2 norm, with the number of bands $\#_B$.

Here, we can state that the above feature vector $\{I_i : i = 1, 2, \dots, \#_B\}$ directly satisfies the invariance for \mathfrak{G}_1 , in light of Property 1 and the translation, rotation and flipping properties of FT. As for scaling, \mathcal{I} is compatible with both single-scale and multi-scale networks: 1) regarding the single-scale case, a certain degree of robustness is provided for \mathfrak{G}_2 (at least up to the bandwidth), in light of Property 2 and the scaling property of FT; 2) regarding the multi-scale case, the scaling covariance has been eliminated before feeding into \mathcal{I} , and thus will satisfy the joint invariance for $\mathfrak{G}_0 = \mathfrak{G}_1 \times \mathfrak{G}_2$.

Note that the well-known average pooling is in fact a special case of (A17), with $K = 0$ and $\#_B = 1$. Our frequency-band integral \mathcal{I} can be regarded as a generic design of global pooling, with comprehensive consideration on interpretability, invariance, and discriminability.

A7. Implementation Details of Experiments/Applications

All experiments/applications are executed in Matlab R2023a under Microsoft Windows environment, based on 2.90-GHz CPU, RTX-3060 GPU, and 16-GB RAM.

Experiment: Our HIR is implemented here as a single-scale network, where scale parameter $w = 10$ and composition length $L = 6$; its invariant layer (A17) is specialized to the average pooling, with $K = 0$ and $\#_B = 1$, for a fair comparison with the deep representations by average pooling. Note that the adaptability strategies of Section 3.2 are not employed here, for a direct assessment of its discriminative power. All features are fed into a PCA classifier, trained on features of the training set. Unless otherwise stated, the training and testing sets are formed without any crossover by random sampling at 80% and 20% ratios on the original dataset, respectively.

Application: Our HIR is implemented here as a single-scale network, where scale parameter $w = 10$ and composition length $L = 7$; its invariant layer (A17) is specialized with $K = N_{ij}/2$ and $\#_B = 30$, for improving the discriminability of digital artifacts. Note that the feature/architecture selection strategy of Section 3.2 is employed for data adaptability and discriminability, where the top-ranked 500- and 1000-dimensional features are selected for AIGC and adversarial perturbation, respectively. All features are fed into both NN and SVM classifiers, for evaluating the sensitivity w.r.t. the classifier. Unless otherwise stated, the training and testing sets are formed without any crossover by random sampling at 50% and 50% ratios on the original dataset, respectively.

Table A1. Classification scores (%) and runtime (second) for different representations on a small-scale texture benchmark.

Method	Time GPU†	Original			Orien. & Flip.		
		Pre.	Rec.	F1	Pre.	Rec.	F1
<i>Classical:</i>							
Cosine	5	70.74	67.50	66.85	69.65	66.25	65.30
Wavelet	6	69.43	64.38	64.68	62.34	58.13	57.82
Kraw.	5	70.67	67.50	66.30	64.41	60.00	59.55
<i>Learning:</i>							
SimpleNet	52†	70.33	67.50	67.09	54.63	43.13	41.31
SimpleNet+	52†	46.93	49.38	46.06	47.18	48.13	44.93
AlexNet	42†	98.82	98.75	98.75	91.69	91.25	91.28
AlexNet+	41†	87.61	84.38	84.05	88.37	85.63	85.76
VGGNet	266†	99.41	99.38	99.37	92.18	91.25	91.37
VGGNet+	609†	91.34	90.00	89.81	92.15	91.25	91.08
<i>Invariant:</i>							
ScatterNet	42	98.89	98.75	98.75	84.98	83.13	83.08
HIR	27	96.98	96.88	96.87	96.32	96.25	96.23

A8. Supplementary Experiments/Applications

A8.1. Texture Experiments

As shown in Fig. 4, the experiment is executed on dataset KTH-TIPS¹, a typical benchmark for texture image classification. This dataset has 10 classes, each containing 81 instances, the total size is $10 \times 81 = 810$, and hence is considered as a small-scale vision problem.

As shown in Table A1, we list performance scores of the competing representations on this benchmark, as well as the elapsed time, *i.e.*, CPU featuring time or GPU training time. Besides this direct protocol on the original dataset, we also consider testing image variants with random orientation (*w.r.t.* $\{0, 90, 180, 270\}$ degree) or flipping (*w.r.t.* x or y axis).

- The classical (over-)complete representations fail to achieve a satisfactory level of discriminability, even in the direct protocol of such small-scale benchmark.
- The learning CNN family achieves significantly higher scores due to its over-complete and data-adaptive properties, especially the AlexNet and VGGNet with large-scale pre-training and transfer learning. Whereas, the SimpleNet performs relatively poorly, indicating the sensitivity of learning to network size and training strategy. Under the variant protocol, they exhibit a significant performance degradation, suggesting the learned features lack invariance *w.r.t.* natural geometric variations of texture. After introducing the augmented training, the CNN scores become more stable, but at the cost of discriminability. A potential reason for this phenomenon is the small amount of training data. Moreover, the computational cost is considerable for this small-scale problem, and a certain training instability is observed.

¹<https://www.csc.kth.se/cvap/databases/kth-tips/index.html>

Table A2. Classification scores (%) and runtime (second, for train./test. = 8/2) for different representations on a large-scale parasite benchmark.

Method	Time GPU†	Train./Test. = 8/2			Train./Test. = 1/9		
		Pre.	Rec.	F1	Pre.	Rec.	F1
<i>Classical:</i>							
Cosine	37	36.19	32.60	29.85	49.40	41.97	43.80
Wavelet	39	41.68	45.20	41.79	53.69	47.97	49.27
Kraw.	42	66.56	69.49	67.21	71.60	57.88	61.10
<i>Learning:</i>							
SimpleNet	2244†	90.15	89.25	89.65	84.51	76.14	78.84
AlexNet	1796†	98.87	98.40	98.63	95.92	94.69	95.27
VGGNet	9184†	99.24	98.97	99.11	97.95	97.37	97.65
<i>Invariant:</i>							
ScatterNet	1277	68.41	69.71	67.55	72.52	63.30	65.70
HIR	823	88.73	92.18	90.10	91.26	88.76	89.85

- The scattering networks provide a high level of discriminability and robustness without feature training and data augmentation, indicating the success of extending classical wavelets to deep representations.
- Our work further extends such success: the HIR achieves a similar level of discriminability as the learning CNN family, while exhibiting superior robustness in the variant protocol than all competing representations. In particular, such representation success build on our compact and efficient framework, with lower runtimes than scattering networks and learning CNN family.

A8.2. Parasite Experiments

As shown in Fig. 4, the experiment is executed on micro-graphic dataset², a typical benchmark for parasite image classification. This dataset has 6 parasite classes and 2 host classes, with real-world diversity regarding imaging, background, morphology, and geometry, the total size is 34298, and hence is considered as a large-scale vision problem.

As shown in Table A2, we list performance scores and elapsed times of the competing representations on this benchmark. Note that we also consider a protocol with different training-testing ratios to analyze the data dependence and sample efficiency.

- In this large-scale problem, the scores of the classical representations drop further, implying a limited level of discriminability. On the other hand, their performance is relatively stable when training samples are reduced, and even better in the 1/9 case, indicating a good efficiency.
- In the learning CNN family, the direct-learning SimpleNet exhibits a clear data dependence. Specifically, it achieves $\sim 90\%$ scores in the 8/2 case (similar to HIR), while the scores drop significantly in the 1/9 case (below than HIR). In contrast, the AlexNet and VGGNet achieve

²<https://data.mendeley.com/datasets/38jtn4nzs6/3>

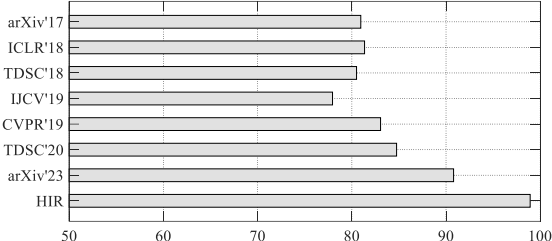


Figure A1. A comparison of adversarial perturbation forensic scores (F1, %) w.r.t. current forensic solutions on the UP benchmark.

good discriminability and stability in the 1/9 case, revealing that the transfer strategy effectively inherits the pre-training prior on ImageNet. On the other hand, the cost of pre-training and transfer learning is still considerable, without guaranteed robustness or adaptability for a given data domain.

- Despite outperforming the original wavelets, scattering networks fail to provide a competitive discriminability in the era of deep learning. Here, the common failure of such hand-crafted representations on larger-scale discriminability can be regarded as important evidence for our motivation.
- The HIR achieves a SimpleNet-level discriminability, outperforming our competitor scattering networks significantly. Also, the HIR is not sensitive to the reduction of training samples, outperforming the learning CNN family in data dependence and sample efficiency. Note that the discriminability of the fixed features from HIR is still lower than the transfer learning with large-scale pre-training. Therefore, in the next applications, the HIR features will be empowered with data adaptability strategies in Section 3.2.

A8.3. Adversarial Perturbation Forensic Applications

As shown in Fig. 5, the dataset ImageNet³ is perturbed through 6 adversarial methods⁴, i.e., BIM [17], CW [7], Damage [8], FGSM [16], PGD [21], and UP [23], respectively, resulting in 6 benchmarks, each containing 5000 clean images and 5000 perturbed versions. This task exhibits real-world discriminative challenges, in light of the rich variability of the perturbations themselves and the underlying ImageNet.

In Fig. A1, we first provide a comparison with the current solutions of perturbation forensics on the basic and realistic UP benchmark. Despite the fixed perturbation pattern, there are still competing methods failing to achieve good scores. Such methods are with under-complete repre-

Table A3. Adversarial perturbation forensic scores (F1, %) for different representations w.r.t. various types of perturbations.

Method	BIM	CW	DAmage	FGSM	PGD	UP	Avg	Min
<i>Classical:</i>								
Cosine NN	34.63	33.19	90.78	39.80	34.69	2.22	39.22	2.22
Cosine SVM	79.57	83.34	97.26	78.24	79.22	96.68	85.72	78.24
Wavelet NN	0.00	0.00	0.00	0.00	0.00	0.00	0.00	0.00
Wavelet SVM	72.83	82.09	97.77	78.21	71.80	95.87	83.10	71.80
Kraw. NN	66.43	66.49	90.86	66.43	66.44	0.00	59.44	0.00
Kraw. SVM	0.00	55.87	0.00	56.44	0.00	70.37	30.45	0.00
<i>Learning:</i>								
SimpleNet	4.24	3.24	92.13	49.89	33.13	99.86	47.08	3.24
AlexNet	90.20	72.72	96.63	94.61	90.91	98.45	90.59	72.72
VGGNet	96.04	62.50	99.08	98.12	96.99	99.15	91.98	62.50
GoogLeNet	90.29	80.04	97.09	95.29	89.94	98.75	91.90	80.04
ResNet	90.22	75.59	97.35	94.66	90.17	98.40	91.07	75.59
DenseNet	98.93	90.19	99.34	99.23	98.85	99.76	97.72	90.19
InceptionNet	98.70	85.14	97.38	97.32	98.66	99.41	96.10	85.14
MobileNet	92.51	82.67	97.37	96.81	92.10	98.19	93.27	82.67
<i>Invariant:</i>								
ScatterNet NN	81.30	70.23	95.27	91.17	82.65	94.64	85.88	70.23
ScatterNet SVM	84.40	69.49	96.77	90.57	83.86	95.12	86.70	69.49
HIR NN	89.66	84.92	98.89	93.26	90.08	97.78	92.43	84.92
HIR SVM	92.30	89.10	99.30	95.96	91.60	98.93	94.53	89.10

sentations, and thereby unable to comprehensively capture perturbation patterns. In contrast, over-complete arXiv'23 and our HIR all achieve > 90% scores, further revealing the fundamental role of representation in forensic tasks. Thus, we will next further compare relevant representation strategies.

In Table A3, we train and test all representations on the 6 benchmarks, presenting the corresponding F1 scores, as well as the average and worst score statistics. This protocol exhibits richer intra-class variability over the fixed perturbation.

- The frequency difference between natural and perturbed data is a fruitful forensic clue. Therefore, the classical (time)-frequency representations achieve higher scores than generally expected on this large-scale problem. However, such features exhibit significant sensitivity to classifiers. A potential reason is the restricted separability, where one must resort to complex classification strategies in the feature space.
- In the learning CNN family, all large-scale networks exhibit > 90% average scores, especially DenseNet and InceptionNet. The phenomenon suggests that the transfer learning is good at capturing discriminative features with sufficient training data and aligned testing protocol. As for the attacks, the CW is more challenging and dominates the worst scores, mainly due to its variable and weak patterns.
- The scattering networks achieve similar scores and much better classifier stability than the original wavelets, suggesting an improvement in the separability. However, its average scores did not reach 90%, failing to provide a similar level of discriminability as learning CNNs.
- Our HIR is very robust to classifier changes, also achieving a MobileNet-level of discriminability, slightly lower

³<https://www.image-net.org/>

⁴<https://github.com/Harry24k/adversarial-attacks-pytorch>

Table A4. Adversarial perturbation forensic scores (%) for different representations on a real-world (hybrid) benchmark.

Method	Train./Test. = 5/5			Train./Test. = 1/9		
	Pre.	Rec.	F1	Pre.	Rec.	F1
<i>Classical:</i>						
Cosine NN	0.00	0.00	0.00	0.00	0.00	0.00
Cosine SVM	79.08	73.33	76.10	81.13	68.79	74.45
Wavelet NN	0.00	0.00	0.00	0.00	0.00	0.00
Wavelet SVM	77.53	66.95	71.85	76.05	61.13	67.78
Kraw. NN	50.53	15.22	23.40	50.00	15.10	23.20
Kraw. SVM	50.03	65.34	56.67	49.75	48.77	49.26
<i>Learning:</i>						
SimpleNet	47.31	48.11	47.71	50.59	63.63	56.36
AlexNet	81.46	87.35	84.30	72.24	61.36	66.35
VGGNet	81.41	90.04	85.51	78.83	75.35	77.05
GoogLeNet	82.74	85.46	84.08	63.35	57.74	60.42
ResNet	80.93	84.70	82.77	68.48	66.64	67.55
DenseNet	87.92	93.25	90.51	82.07	83.96	83.00
InceptionNet	84.60	90.92	87.65	69.58	70.77	70.17
MobileNet	83.07	88.07	85.50	68.73	69.50	69.11
<i>Invariant:</i>						
Scatter. NN	69.85	68.94	69.39	74.93	77.31	76.10
Scatter. SVM	75.70	72.07	73.84	76.42	78.63	77.51
HIR NN	81.27	80.68	80.98	79.09	82.17	80.60
HIR SVM	86.20	86.06	86.13	83.42	83.29	83.35

than DenseNet and InceptionNet, and significantly better than the direct competitor scattering networks. Therefore, our strategy has a better combined performance in robustness, interpretability, and discriminability. Its efficiency benefit will be highlighted in the next experimental protocol.

In Table A4, we train and test all representations on a hybrid of the 6 perturbation benchmarks, presenting scores at two training-testing ratios. This protocol is more challenging due to very complex intra-class variability, while being more practical for real-world forensic scenarios.

- In line with previous observations, the classical representations still exhibit score fluctuations on the two classifiers. We also note a performance degradation compared to the case of Table A3, due to the discriminative challenges by this hybrid protocol. On the other hand, their performance is stable *w.r.t.* the reduction of training samples, further validating the inherent advantages in sample efficiency.
- Moving into this hybrid benchmark, the learning CNN family yields consistent and large performance degradation, especially for the 1/9 case with fewer samples. This phenomenon is direct evidence for the data dependence in learning representations (even with transfer strategy). In fact, real-world forensics often face the situation where the perturbation types are diverse and some of them lack samples. Therefore, such data-dependent forensics typically exhibit time-consuming (re-)training, while failing

to guarantee their validity for under-sampled perturbation patterns.

- The scattering networks basically continue the discriminability level and classifier stability from Table A3. Note that its scores in the 1/9 case are higher than most classical and learning representations, reflecting the superior performance in both discriminability and efficiency.
- In this challenging protocol, the hand-crafted HIR still achieves a learning-level discriminability and consistently outperforms scattering networks. More importantly, our HIR is significantly less dependent on training samples than learning CNNs, meaning it can better cope with under-sampled perturbation patterns in practice. For the AIGC forensic task, the comprehensive advantages of HIR over learning CNNs will be further highlighted, in robustness, interpretability, discriminability, and efficiency.

References

- [1] Joakim Andén and Stéphane Mallat. Deep scattering spectrum. *IEEE Trans. Signal Process.*, 62(16):4114–4128, 2014. [1](#)
- [2] Kenneth Atz, Francesca Grisoni, and Gisbert Schneider. Geometric deep learning on molecular representations. *Nature Mach. Intell.*, 3(12):1023–1032, 2021. [1](#)
- [3] V Balntas, K Lenc, A Vedaldi, T Tuytelaars, J Matas, and K Mikolajczyk. H-Patches: A benchmark and evaluation of handcrafted and learned local descriptors. *IEEE Trans. Pattern Anal. Mach. Intell.*, 42(11):2825–2841, 2019. [1](#)
- [4] Erik J Bekkers. B-spline CNNs on Lie groups. In *Proc. Int. Conf. Learn. Representations*, 2019. [1](#)
- [5] Joan Bruna and Stéphane Mallat. Invariant scattering convolution networks. *IEEE Trans. Pattern Anal. Mach. Intell.*, 35(8):1872–1886, 2013. [1, 4](#)
- [6] Cameron Buckner. Understanding adversarial examples requires a theory of artefacts for deep learning. *Nature Mach. Intell.*, 2(12):731–736, 2020. [1](#)
- [7] Nicholas Carlini and David Wagner. Towards evaluating the robustness of neural networks. In *Proc. IEEE Symp. Secur. Privacy*, pages 39–57, 2017. [7](#)
- [8] Sizhe Chen, Zhengbao He, Chengjin Sun, Jie Yang, and Xiaolin Huang. Universal adversarial attack on attention and the resulting dataset DamageNet. *IEEE Trans. Pattern Anal. Mach. Intell.*, 44(4):2188–2197, 2020. [7](#)
- [9] Xu Chen, Xiuyuan Cheng, and Stéphane Mallat. Unsupervised deep Haar scattering on graphs. *Proc. Adv. Neural Inf. Process. Syst.*, 27, 2014. [1](#)
- [10] Siyao Cheng, Yuan-Sen Ting, Brice Ménard, and Joan Bruna. A new approach to observational cosmology using the scattering transform. *Mon. Not. R. Astron. Soc.*, 499(4):5902–5914, 2020. [1](#)
- [11] Taco Cohen and Max Welling. Group equivariant convolutional networks. In *Proc. Int. Conf. Mach. Learn.*, pages 2990–2999, 2016. [4](#)
- [12] Taco S Cohen and Max Welling. Steerable CNNs. In *Proc. Int. Conf. Learn. Representations*, 2016. [1](#)

- [13] Marc Finzi, Samuel Stanton, Pavel Izmailov, and Andrew Gordon Wilson. Generalizing convolutional neural networks for equivariance to Lie groups on arbitrary continuous data. In *Proc. Int. Conf. Mach. Learn.*, pages 3165–3176, 2020. 1
- [14] Jan Flusser, Barbara Zitova, and Tomas Suk. *Moments and moment invariants in pattern recognition*. John Wiley & Sons, 2009. 5
- [15] Kunihiko Fukushima and Sei Miyake. Neocognitron: A new algorithm for pattern recognition tolerant of deformations and shifts in position. *Pattern Recognit.*, 15(6):455–469, 1982. 1
- [16] Ian J Goodfellow, Jonathon Shlens, and Christian Szegedy. Explaining and harnessing adversarial examples. *arXiv preprint arXiv:1412.6572*, 2014. 7
- [17] Alexey Kurakin, Ian J Goodfellow, and Samy Bengio. Adversarial examples in the physical world. In *Artificial Intelligence Safety and Security*, pages 99–112. Chapman and Hall/CRC, 2018. 7
- [18] Yann LeCun, Yoshua Bengio, and Geoffrey Hinton. Deep learning. *Nature*, 521(7553):436–444, 2015. 1
- [19] Karel Lenc and Andrea Vedaldi. Understanding image representations by measuring their equivariance and equivalence. In *Proc. IEEE Conf. Comput. Vis. Pattern Recognit.*, pages 991–999, 2015. 2
- [20] David G Lowe. Distinctive image features from scale-invariant keypoints. *Int. J. Comput. Vis.*, 60:91–110, 2004. 1
- [21] Aleksander Madry, Aleksandar Makelov, Ludwig Schmidt, Dimitris Tsipras, and Adrian Vladu. Towards deep learning models resistant to adversarial attacks. In *Proc. Int. Conf. Learn. Representations*, 2018. 7
- [22] Diego Marcos, Michele Volpi, Nikos Komodakis, and Devis Tuia. Rotation equivariant vector field networks. In *Proc. IEEE Int. Conf. Comput. Vis.*, pages 5048–5057, 2017. 2
- [23] Seyed-Mohsen Moosavi-Dezfooli, Alhussein Fawzi, Omar Fawzi, and Pascal Frossard. Universal adversarial perturbations. In *Proc. IEEE Conf. Comput. Vis. Pattern Recognit.*, pages 1765–1773, 2017. 7
- [24] Edouard Oyallon, Sergey Zagoruyko, Gabriel Huang, Nikos Komodakis, Simon Lacoste-Julien, Matthew Blaschko, and Eugene Belilovsky. Scattering networks for hybrid representation learning. *IEEE Trans. Pattern Anal. Mach. Intell.*, 41(9):2208–2221, 2018. 1
- [25] Shuren Qi, Yushu Zhang, Chao Wang, Jiantao Zhou, and Xiaochun Cao. A survey of orthogonal moments for image representation: theory, implementation, and evaluation. *ACM Comput. Surv.*, 55(1):1–35, 2021. 1, 2, 3, 5
- [26] Shuren Qi, Yushu Zhang, Chao Wang, Jiantao Zhou, and Xiaochun Cao. A principled design of image representation: Towards forensic tasks. *IEEE Trans. Pattern Anal. Mach. Intell.*, 45(5):5337–5354, 2022. 2, 3, 4
- [27] Shuren Qi, Yushu Zhang, Chao Wang, Tao Xiang, Xiaochun Cao, and Yong Xiang. Representing noisy image without denoising. *IEEE Transactions on Pattern Analysis and Machine Intelligence*, 2024. 4
- [28] Olga Russakovsky, Jia Deng, Hao Su, Jonathan Krause, Sanjeev Satheesh, Sean Ma, Zhiheng Huang, Andrej Karpathy, Aditya Khosla, Michael Bernstein, et al. ImageNet large scale visual recognition challenge. *Int. J. Comput. Vis.*, 115: 211–252, 2015. 1
- [29] Laurent Sifre and Stéphane Mallat. Rotation, scaling and deformation invariant scattering for texture discrimination. In *Proc. IEEE Conf. Comput. Vis. Pattern Recognit.*, pages 1233–1240, 2013. 1
- [30] Ivan Sosnovik, Michał Szmaja, and Arnold Smeulders. Scale-equivariant steerable networks. In *Proc. Int. Conf. Learn. Representations*, 2019. 1
- [31] Zikai Sun and Thierry Blu. Empowering networks with scale and rotation equivariance using a similarity convolution. In *Proc. Int. Conf. Learn. Representations*, 2023. 1
- [32] Mariarosaria Taddeo, Tom McCutcheon, and Luciano Floridi. Trusting artificial intelligence in cybersecurity is a double-edged sword. *Nature Mach. Intell.*, 1(12):557–560, 2019. 1
- [33] Engin Tola, Vincent Lepetit, and Pascal Fua. Daisy: An efficient dense descriptor applied to wide-baseline stereo. *IEEE Trans. Pattern Anal. Mach. Intell.*, 32(5):815–830, 2009. 1
- [34] Raphael JL Townshend, Stephan Eismann, Andrew M Watkins, Ramya Rangan, Masha Karelina, Rhiju Das, and Ron O Dror. Geometric deep learning of RNA structure. *Science*, 373(6558):1047–1051, 2021. 1
- [35] Maurice Weiler, Fred A Hamprecht, and Martin Storath. Learning steerable filters for rotation equivariant CNNs. In *Proc. IEEE Conf. Comput. Vis. Pattern Recognit.*, pages 849–858, 2018. 1
- [36] Thomas Wiatowski and Helmut Bölcskei. A mathematical theory of deep convolutional neural networks for feature extraction. *IEEE Trans. Inf. Theory*, 64(3):1845–1866, 2017. 1
- [37] Daniel Worrall and Max Welling. Deep scale-spaces: Equivariance over scale. *Proc. Adv. Neural Inf. Process. Syst.*, 32, 2019. 1
- [38] Daniel E Worrall, Stephan J Garbin, Daniyar Turmukhambetov, and Gabriel J Brostow. Harmonic networks: Deep translation and rotation equivariance. In *Proc. IEEE Conf. Comput. Vis. Pattern Recognit.*, pages 5028–5037, 2017. 1
- [39] Qi Xie, Qian Zhao, Zongben Xu, and Deyu Meng. Fourier series expansion based filter parametrization for equivariant convolutions. *IEEE Trans. Pattern Anal. Mach. Intell.*, 45(4):4537–4551, 2022. 1
- [40] Pew-Thian Yap, Xudong Jiang, and Alex Chichung Kot. Two-dimensional polar harmonic transforms for invariant image representation. *IEEE Trans. Pattern Anal. Mach. Intell.*, 32(7):1259–1270, 2009. 5
- [41] Sunkyu Yu. Evolving scattering networks for engineering disorder. *Nature Comput. Sci.*, 3(2):128–138, 2023. 1
- [42] Richard Zhang. Making convolutional networks shift-invariant again. In *Proc. Int. Conf. Mach. Learn.*, pages 7324–7334, 2019. 1, 3